Keynote Topic

This article is part of the **Oxide Electronics**
keynote topic compilation.

Nanoscale Phenomena in Oxide Heterostructures

Joseph A. Sulpizio,[1] Shahal Ilani,[1] Patrick Irvin,[2]
and Jeremy Levy[2]

[1]Department of Condensed Matter Physics, Weizmann Institute of Science, Rehovot 76100,
Israel; email: joseph.sulpizio@weizmann.ac.il, shahal.ilani@weizmann.ac.il

[2]Department of Physics and Astronomy, University of Pittsburgh, Pittsburgh,
Pennsylvania 15260; email: prist2@pitt.edu, jlevy@pitt.edu

Keywords

complex oxides, scanning probe microscopy, strongly correlated electrons

Abstract

Recent advances in creating complex oxide heterostructures, interfaces
formed between two different transition-metal oxides, have heralded a new
era of materials and physics research, enabling a uniquely diverse set of co-
existing physical properties to be combined with an ever-increasing degree
of experimental control. These systems have exhibited varied phenomena
such as superconductivity, magnetism, and ferroelasticity, all of which are
gate tunable, demonstrating their promise for fundamental discovery and
technological innovation. To fully exploit this richness, it is necessary to
understand and control the physics on the smallest scales, making the use of
nanoscale probes essential. Using the prototypical $LaAlO_3/SrTiO_3$ interface
as a guide, we explore the exciting developments in the physics of oxide-based
heterostructures, with a focus on nanostructures and the nanoscale probes
employed to unravel their complex behavior.

1. INTRODUCTION

For many decades, a sharp dichotomy has persisted between the study of quantum materials and the study of semiconductor/mesoscopic physics. The major thrust in the field of quantum materials has been the development and study of bulk, 3D correlated systems, in which many physical phenomena can be achieved within a single materials family. A particularly fruitful family is that of the complex (transition-metal) oxides. Varying the composition and arrangement of the metal atoms in these oxides has enabled the synthesis of a diverse array of materials, including high-temperature superconductors, quantum magnets, ferroelectrics, and multiferroics. Meanwhile, the field of semiconductor physics has focused primarily on developing control over the dimensionality, cleanliness, and geometry of functional devices. Over the past ten years, these formerly independent communities have begun to overlap, beginning with the discovery of a high-mobility 2D electron gas (2DEG) living at the interface between strontium titanate ($SrTiO_3$) and lanthanum aluminate ($LaAlO_3$) (1). This emerging field of complex oxide heterostructures, devices made by combining different transition-metal oxides, has enabled researchers to apply the experimental flexibility and tools of semiconductor physics to a family of materials that exhibits a multitude of intriguing physical properties.

The target audience for this review consists of researchers in mesoscopic physics, quantum transport, device engineering, and quantum information who are interested in this burgeoning field. Until recently, the main advances in this new field were made by traditional materials science–based approaches. However, as complex oxide heterostructures reach an ever-higher degree of maturity, researchers employing a broader class of approaches, from fundamental quantum physics to device applications, can find fertile ground for discovery.

To appreciate the potential novelty of oxide heterointerfaces, in **Table 1** we highlight a selection of their properties compared with those in other flagship solid-state systems. Clearly, oxide interfaces are not yet as electronically clean as these other systems (although the quality of oxide interfaces is rapidly improving). However, their origin in strongly correlated materials endows these interfaces with a large set of properties that are rarely found to coexist in conventional materials systems. These properties include gate-tunable magnetism that persists to room temperature, intrinsic superconductivity, strong spin-orbit interactions, electron-lattice interactions, and possibly even ferroelectricity. Moreover, these properties have strong interrelationships, which once properly understood can be exploited to realize unique physical systems that have no counterpart in any other materials system.

This review provides an overview of the properties of oxide nanostructures, with an emphasis on the important role that local probes can play in gaining insight into this family of materials. Nanoscale probes have made important contributions to understanding and controlling the microscopic physics in the oxides. Scanning probes were critical in establishing the two-dimensionality of conducting electronic systems living near the interface (2), in identifying the influence of microscopic structural domains on interfacial electrons (3, 4), and in creating unique device architectures down to the nanoscale (5, 6). As becomes clear over the course of this article, with so many different physical effects simultaneously at play in these systems, visualizing and isolating the individual components on microscopic scales are crucial. Thus, nanoscale probes serve an increasingly vital role in the study of the oxides. The prototypical, and most widely studied, oxide heterostructure is $LaAlO_3/SrTiO_3$, and so naturally this particular heterostructure occupies much of the focus of this review. The knowledge gained, however, is endemic to the growing class of related oxide materials.

Table 1 Comparison between $LaAlO_3/SrTiO_3$ and other solid-state materials systems for nanoscale devices. Although $LaAlO_3/SrTiO_3$ is currently more electronically disordered than the other materials systems, its broad array of physical properties and potential tunability make it very attractive as a system for studying correlated electron physics in engineered environments

	$LaAlO_3/SrTiO_3$	III–V semiconductor heterostructures	Graphene	Nanotubes	Semiconducting nanowires
Dimensionality	2D/1D	2D/1D	2D	1D	1D
Record mobility $[cm^2/(V \cdot s)]$	6,600 (82)[a]	36,000,000 (162, 163)	200,000 (164–166)	>100,000 (167)	20,000 (168)
Mean free path	Hundreds of nanometers	~100 μm	~1 μm (165)	On substrate: ~10 μm (169); suspended: not yet measured	~100 nm (170)
Typical densities	10^{12}–10^{14} cm^{-2}	10^{10}–10^{12} cm^{-2}	10^9–5×10^{12} cm^{-2}	10^3–10^8 cm^{-1}	10^5–10^8 cm^{-1}
Achievable lithographic feature size	A few nanometers with AFM lithography	~100 nm [limited by interface depth (171)]	A few nanometers (but with substantially increasing disorder)	Tens of nanometers [disorder-free in suspended devices (172)]	A few nanometers (grown heterointerfaces along wires)
Superconductivity	Yes; $T_c^{max} \sim$ 300 mK; gate tunable	No	No (only by proximity)	No (only by proximity)	No (only by proximity)
Magnetism	Yes; $T_c > 300$ K (22, 35); gate tunable	Yes; $T_c < 200$ K (173)	No	No	Yes; $T_c < 20$ K
Ferroelectricity	Possibly	No	No	No	No
Strong lattice-electron coupling	Yes	No	No	Yes	No
Spin-orbit coupling	Yes; a few meV; gate tunable	Yes; ~1 meV; gate tunable; Rashba and Dresselhaus	No; a few μeV; predicted	Yes (174–176); a few meV; circumferential motion coupled to spin	Yes; ~200 μeV; primarily Rashba

[a]A mobility of >100,000 cm^2/(V $\cdot$ s) has been reported in γ-alumina/SrTiO$_3$ (47).

2. SrTiO$_3$: THE UNIVERSAL SUBSTRATE

SrTiO$_3$ is the near-universal substrate on which complex oxide structures are built and from which their properties are largely inherited. Thus, before proceeding to our discussions of nanoscale phenomena in complex oxide heterostructures, we first review the relevant physics of SrTiO$_3$, a material that has been extensively and continuously studied since the 1940s due to its remarkable array of properties. These diverse properties are best appreciated by considering how they emerge through the breaking of fundamental symmetries: point group symmetry (ferroelasticity), charge inversion symmetry (ferroelectricity), U(1) gauge symmetry (superconductivity), and spin rotation symmetry [ferromagnetism (FM)]. We now discuss the specific breaking of each of these

symmetries in the context of $SrTiO_3$, guided by the order in which they emerge as a function of decreasing temperature.

2.1. Broken Symmetries in SrTiO₃

$SrTiO_3$ has a perovskite crystal structure (**Figure 1a**). At room temperature, its unit cell is cubic and composed of an outermost arrangement of eight strontium atoms. Centered on each face of the cube is one of six oxygen atoms, which together form the vertices of an octahedral cage. At the center of this cage lies the titanium atom. This cubic structure gives the most energetically favorable packing of the constituent atoms at high temperatures, but as the temperature is reduced, more efficient packing can be achieved. At $T = 105$ K, neighboring oxygen octahedra rotate in opposite directions (antiferrodistortive transition; **Figure 1b**) to reach the optimal bond lengths between both the strontium-oxygen pairs and the titanium-oxygen pairs (Goldschmidt tolerance) (7, 8). As a result of these rotations, the cubic symmetry is broken, and the unit cell becomes a rectangular prism with one long axis (the *c*-axis) and two short axes (*a*-axes) (**Figure 1b**). This ferroelastic transition naturally leads to the formation of domains within the $SrTiO_3$ with different orthogonal orientations of the tetragonal unit cells (9, 10). Subsequent sections discuss in detail the consequences of this domain structure for nanoscale phenomena, including the effect on local electronic properties of oxide heterostructures. Further lowering of the crystal symmetry into orthorhombic and triclinic structures may occur at lower temperatures, although the magnitude of these additional perturbations is significantly smaller than the aforementioned transition to tetragonal symmetry. All such structural changes in the crystal symmetry lift the orbital degeneracies of the electronic system (11, 12) and thus directly affect the electronic structure of the material.

After the cubic crystal symmetry of $SrTiO_3$ is broken, the next symmetry to break is inversion symmetry. At room temperature, the titanium atom is centered inside the oxygen cage. Only through the application of an external electric field will the titanium atom displace off center, making $SrTiO_3$ a paraelectric material at room temperature. This paraelectric state persists even below the ferroelastic transition. At even lower temperatures, however, the unit cell elongates enough such that a double-well potential develops for the titanium atom, with minima situated near opposite ends of the long axis of the oxygen octahedron (**Figure 1c**). For $SrTi^{18}O_3$, which has the heavier isotope of oxygen, a ferroelectric transition occurs at $T = 23$ K (13): The titanium atom spontaneously displaces toward one of these minima, resulting in a nonzero dipole moment within the unit cell. In contrast, the ^{16}O isotope happens to be just light enough such that even at zero temperature it can quantum-mechanically tunnel between the two potential minima, a phenomenon termed quantum paraelectricity (14). Similar to the case for $SrTi^{18}O_3$, whose dielectric constant diverges at the ferroelectric transition, the dielectric constant of $SrTi^{16}O_3$ also rapidly increases with decreasing temperature. However, this increase is cut off by the quantum tunneling, and this constant plateaus at a high value of $\sim20,000$ (15), signifying the highly polarizable nature of this state. By growing thin films of $SrTiO_3$ on tensile-strained substrates, ferroelectricity can be observed as high as room temperature (16, 17).

Although $SrTiO_3$ is innately a band insulator, it can be made conducting by doping, for example, with niobium. At very low temperatures ($T \sim 300$ mK), another symmetry—the U(1) gauge symmetry of the superconducting order parameter—is broken. Thus, doped $SrTiO_3$ becomes a superconductor (18) (**Figure 1d**), a property shared by many $SrTiO_3$-based oxide heterostructures. Finally, the breaking of rotational symmetry in spin space, which results in FM, was never observed in bulk $SrTiO_3$ at any temperature. However, researchers recently discovered (19) that FM can emerge in $SrTiO_3$-based heterostructures (19–35) and in thin films (36), leading to pronounced
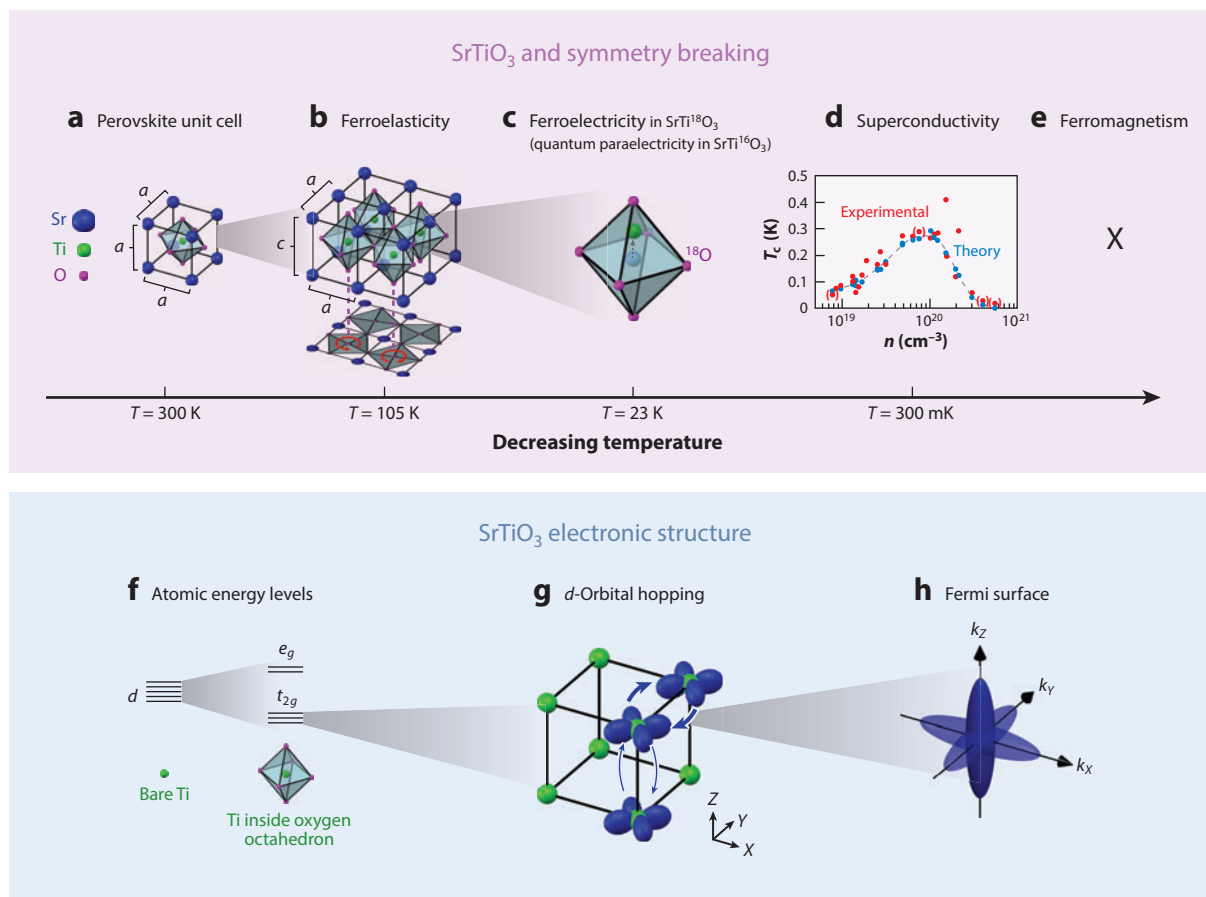
SrTiO$_3$ and symmetry breaking

a Perovskite unit cell **b** Ferroelasticity **c** Ferroelectricity in SrTi^{18}O$_3$ (quantum paraelectricity in SrTi^{16}O$_3$) **d** Superconductivity **e** Ferromagnetism

$T = 300$ K $T = 105$ K $T = 23$ K $T = 300$ mK

Decreasing temperature

SrTiO$_3$ electronic structure

f Atomic energy levels **g** d-Orbital hopping **h** Fermi surface

Figure 1

SrTiO$_3$: the universal substrate. (*a–e*) The physical properties of SrTiO$_3$ emerge through the breaking of various symmetries as the temperature is lowered. (*a*) At room temperature, the perovskite unit cell has cubic symmetry, with three orthogonal *a*-axes of equal length. (*b*) Below $T = 105$ K, a ferroelastic transition to tetragonal crystal symmetry occurs, wherein the crystal has two short *a*-axes and one long *c*-axis. This transition arises from an increasing octahedral tilt, wherein neighboring oxygen octahedra develop a relative rotation (*bottom projection*; *red arrows* indicate rotation). (*c*) A ferroelectric transition occurs for SrTi^{18}O$_3$ at $T = 23$ K, endowing the unit cell with a permanent electric dipole from the displacement of the central titanium atom toward a corner of the distorted oxygen octahedron (*dashed arrow*). Quantum tunneling suppresses this transition for normal SrTi^{16}O$_3$, making it a quantum paraelectric. (*d*) Near $T = 300$ mK, doped SrTiO$_3$ becomes a superconductor (18) whose critical temperature exhibits a dome structure as a function of carrier density. Panel *d* adapted with permission from Reference 18. Copyright 1967, the American Physical Society. (*e*) Rotation symmetry in spin space is always preserved, and therefore bulk SrTiO$_3$ does not exhibit magnetism at any temperature (indicated by the X). (*f–h*) Electronic structure of SrTiO$_3$. (*f*) The electronic orbitals near the Fermi level in SrTiO$_3$ are the fivefold-degenerate titanium *d* orbitals. Once the titanium is surrounded by the oxygen octahedron, the *d* orbitals are split into a higher-energy doublet (e_g states) and a lower-energy triplet (t_{2g} states). (*g*) Electrons located in the t_{2g} orbitals (d_{XY}, d_{YZ}, d_{XZ}) are coupled to identical orbitals on neighboring lattice sites. Hopping matrix elements are much larger in the plane of an orbital's lobes than in the perpendicular direction, illustrated here for the d_{XY} orbitals. The thickness of the arrows indicates that hopping between d_{XY} orbitals (*blue*) is stronger along the *X* and *Y* directions (corresponding to a light effective mass) than along the *Z* direction (corresponding to a heavy effective mass). (*h*) The corresponding Fermi surface is cigar shaped; it is elongated in the k_Z direction for the d_{XY} orbitals (*solid blue*) and is elongated in the k_Y and k_X directions for the d_{XZ} and d_{YZ} orbitals (*transparent blue*), respectively.

magnetic ground states. Remarkably, as discussed in subsequent sections, these magnetic effects coexist with superconductivity (21–23), even though magnetism and superconductivity are generally considered to be mutually exclusive. In fact, at these complex oxide interfaces, all four of the above-mentioned symmetries have mutual interplay, leading to a very rich class of physical systems.

2.2. SrTiO₃ Electronic Structure

Having discussed the relevant symmetries, we now turn to the electronic structure of $SrTiO_3$, from which stem most of the physically observable quantities of complex oxide heterostructures. The energy states most relevant for the low-energy physics of this system, those near the Fermi level, arise from the fivefold-degenerate d orbitals of the titanium atom (**Figure 1f**). This degeneracy is lifted by the surrounding oxygen cage, which splits the levels into a high-energy doublet (e_g states) and a low-energy triplet (t_{2g} states) that remains near the Fermi level. These t_{2g} states are composed of the d_{XY}, d_{XZ}, and d_{YZ} orbitals, which couple to identical orbitals on titanium atoms at neighboring lattice sites through the p orbitals of the oxygen atoms that lie in between. For a given orbital, the hopping matrix elements are much larger in the plane of the lobes than out of the plane of the lobes. For example, for the d_{XY} orbital the hopping is much stronger along the X and Y directions than along the Z direction (**Figure 1g**), and as a result the effective mass is lower along the X and Y directions than it is along the Z direction. In k-space, the lower effective mass leads to a cigar-shaped Fermi surface along the k_Z direction (**Figure 1h**). The d_{XZ} and d_{YZ} orbitals have analogous Fermi surfaces pointing along the k_Y and k_X directions, together forming a threefold band structure centered at the Γ-point in k-space (37). The ferroelastic and ferroelectric distortions discussed above lift the degeneracy of the three t_{2g} orbital, as do spin-orbit interactions and the breaking of inversion symmetry near a surface or an interface. This relation between crystal structure and electronic degeneracies creates interesting degrees of freedom that are still not fully characterized or utilized in these materials.

The coexistence of such diverse phenomena in a single material can at first glance give the impression of a system that is hopelessly complex. However, the same degrees of freedom, if controlled, could lead to the creation of systems with great promise for technological applications and fundamental studies alike. Whereas in the bulk these degrees of freedom can be controlled to a certain extent, the advent of oxide interfaces has allowed for the creation of systems that exploit the fundamental symmetries in entirely new ways, as we explore throughout the remainder of this review.

3. LaAlO₃/SrTiO₃: A CONDUCTING LAYER BETWEEN TWO INSULATORS

Although the discovery that conduction can dramatically emerge at the interface between a thin layer of LaAlO₃ grown on top of SrTiO₃ (**Figure 2a**) has led to a flurry of research on oxide interfaces (38), there remain many fundamental questions about these systems. The most basic question—why a conducting layer appears, given that the two parent materials are insulating—is an outstanding puzzle, and in this section we review the different mechanisms proposed to explain this phenomenon.

3.1. Influence of Growth Conditions

Whether an oxide interface is conductive or insulating is strongly dependent on the growth conditions, giving an important clue to the underlying mechanisms for conductivity. Oxide
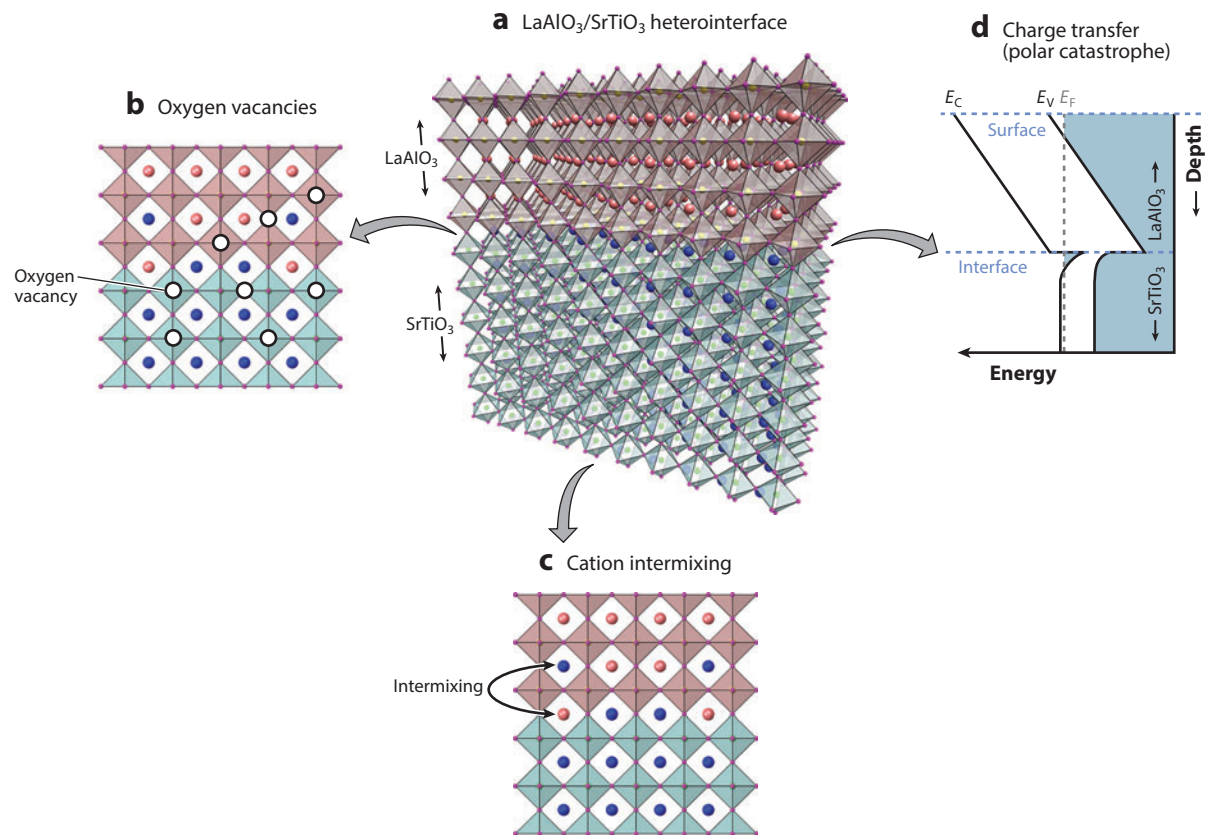
a LaAlO₃/SrTiO₃ heterointerface

b Oxygen vacancies

c Cation intermixing

d Charge transfer (polar catastrophe)

Figure 2

Mechanisms for interfacial conductivity in oxide heterostructures. (*a*) The LaAlO₃/SrTiO₃ heterointerface. Four monolayers of LaAlO₃ are shown atop a thicker SrTiO₃ substrate. The atoms are colored as follows: La (*orange*), Al (*yellow*), Sr (*blue*), Ti (*green*), and O (*purple*). (*b*) Oxygen vacancies may form, donating charge to populate a conducting interface layer. (*c*) Cation intermixing, in which strontium atoms change position with lanthanum atoms across the interface, may also effectively dope the interfacial layer. (*d*) Charge transfer/polar catastrophe: For polar growth orientations [e.g., the (100) orientation], the built-in electric field in LaAlO₃ raises the energy of its bands with each layer. Beyond a critical LaAlO₃ thickness of 3 unit cells, the LaAlO₃ valence band edge of the top layer reaches the energy of the SrTiO₃ conduction band edge, and charge is transferred from the surface to the interface, populating a conducting interfacial layer. The energy bands are shown schematically. The Fermi level is marked by the vertical, dashed, gray line. The shaded regions represent occupied electron states, showing an excess of electron charge density in the SrTiO₃ conduction band near the LaAlO₃/SrTiO₃ interface; the excess electrons are donated from formerly occupied electron states at the surface, where an excess of holes now remains.

heterostructures, and specifically LaAlO₃/SrTiO₃, are grown primarily by pulsed laser deposition (PLD), although molecular beam epitaxy (MBE), chemical vapor deposition (CVD), and sputtering are used as well. The most-studied interface to date is that of crystalline LaAlO₃ grown over the (100) surface of SrTiO₃. Along this growth direction, the SrTiO₃ is composed of alternating layers of TiO_2 and SrO, both of which are charge neutral. In contrast, LaAlO₃ grown along this direction is polar and consists of alternating layers of LaO and AlO_2, which have a charge of $+1$ and -1 per unit cell, respectively. This arrangement results in a sharp transition at the interface between a nonpolar material and a polar material. First, a conducting interface is achieved only when SrTiO₃ is terminated with a TiO_2 plane, and not with an SrO plane (39). Moreover, the

conductivity abruptly emerges only when the $LaAlO_3$ thickness reaches a critical value of 4 unit cells (40). $LaAlO_3$ stoichiometry (41–44), oxygen partial pressure during growth, and thermal annealing (40) have an important influence on interface conductivity. Growth along the (111) direction, whose polar discontinuity is different from that of the (100) direction, and growth along the (110) direction, which has no discontinuity, have also exhibited conducting interfaces beyond a critical thickness, although in these cases it is not clear whether the critical thickness is universal, as it is along the (100) direction. Nonpolar overlayers such as amorphous $LaAlO_3$ (45, 46) and spinel γ-alumina (47) also lead to interfacial conductivity, sometimes with exceptionally high mobility (47). However, in contrast to the $LaAlO_3/SrTiO_3$ case, here the conductivity disappears with annealing in oxygen. Finally, even the surface of bare $SrTiO_3$ can be made to conduct, either by top gating of $SrTiO_3$ (48–51) or by cleaving $SrTiO_3$ in vacuum (52, 53).

For all these interfaces, establishing whether the conductivity occurs in the 3D bulk of $SrTiO_3$ or through a 2D layer near the interface (i.e., a 2DEG) has been of primary interest. Here, nanoscale probes have played an essential role. By using conductive-tip atomic force microscopy (AFM), the location of the conducting electrons was directly imaged in cross sections of $LaAlO_3/SrTiO_3$ (2). These measurements revealed that conduction in samples grown under oxygen-poor conditions occurs throughout the bulk of the $SrTiO_3$; however, after oxygen annealing, such conduction is concentrated in a narrow (<7-nm) region below the interface. Cross-sectional scanning tunneling microscopy (STM) studies on $LaAlO_3/SrTiO_3$ also measured a narrow (~0.8-nm) 2D metallic region (54), as did magnetotransport studies, which are discussed in the next section.

3.2. Mechanisms for Interfacial Conduction

The above observations have led to conflicting views on the mechanisms generating conductivity at the interface, and this topic remains hotly debated. Oxygen vacancies in $SrTiO_3$ (**Figure 2b**) can act as electron donors (55). The energetic barrier for the formation of these defects is quite low compared with, for example, the energetic barrier for the formation of defects in semiconductors, and formation in the former case may be further enhanced by fields near the interface (56). The observed sensitivity of interface conductivity to oxygen pressure during growth and to annealing supports this scenario. Cation intermixing across the interface in which atoms of different valence are exchanged may also play an important role (57, 58). For example, lanthanum atoms readily dope bulk $SrTiO_3$, and thus their interchange with strontium atoms across the interface may lead to local doping and to the generation of a conducting layer (**Figure 2c**). Transmission electron microscopy (39) and surface X-ray diffraction studies (59) showed that the interface is not always atomically sharp, hinting that this scenario may be relevant.

However, there is a fundamental intrinsic mechanism based on the presence of a strong polar discontinuity at the interface (60–62) that is often termed the polar catastrophe (39). For growth orientations that involve a polar discontinuity, the potential difference across the $LaAlO_3$ increases linearly with its thickness, lifting the energy of its valence band with each additional monolayer (63–65). At a critical layer thickness, this band crosses the Fermi level, and it then becomes energetically favorable to transfer electrons from the $LaAlO_3$ valence band edge at the surface to the bottom of the $SrTiO_3$ conduction band near the interface. The field generated by additional $LaAlO_3$ monolayers beyond this critical thickness is compensated for by further charge transfer from the surface to the interface, effectively pinning the surface $LaAlO_3$ valence band edge to the Fermi level. This charge transfer naturally results in the formation of a conducting 2D layer near the interface (**Figure 2d**). In contrast to the above-mentioned scenarios, which rely on local dopants that can be randomly distributed and that are located close to the interface, the polar catastrophe scenario is reminiscent of field-effect gating, in which charge is transferred from a spatially separated,

homogeneous region. Conducting layers generated by this mechanism could be made free of disorder, assuming that one could eliminate other imperfections in the underlying lattice.

Strong support for the relevance of the polar catastrophe scenario comes from the fact that the observed critical thickness for conductivity in (100) $LaAlO_3/SrTiO_3$ is universal across many labs throughout the world employing a variety of growth techniques and conditions. However, the polar catastrophe scenario also suggests that a hole gas should form at the $LaAlO_3$ surface from the vacancies created by the charge donated to the interface, and evidence of this hole gas has not been seen experimentally so far. Furthermore, the other mechanisms outlined above may also be sensitive to local polarization fields that may lead to very similar critical thickness dependence (56). The various scenarios described above are not mutually exclusive, and under generic growth conditions, multiple mechanisms may be at play. A systematic growth study (66) across the parameter space in which oxygen vacancy formation and charge transfer (polar catastrophe) are expected to be relevant indeed demonstrated how different mechanisms can coexist. With an improved understanding and control over sample growth, it may be possible in the future to tailor the interface electrical properties on the basis of a choice of a particular mechanism for the formation of the conducting layer.

In addition to controlling conducting interfaces via growth conditions, tuning the conductivity in situ through a variety of approaches is also possible. Such tunability gives oxide heterostructures a great advantage over bulk oxides. Most prominently, the charge density of the 2D conducting layer can be tuned through the electric field effect by the application of both back-gate and top-gate voltages (40, 67). Reversibly changing the interfacial conductivity using ferroelectric layers grown above $LaAlO_3$ is also possible. Applied to an $LaAlO_3/SrTiO_3$ sample just below the critical thickness, this approach (68) enables switching between insulating phases and conducting phases. Polar adsorbates such as acetone and ethanol also influence the conductive properties of $LaAlO_3/SrTiO_3$ heterostructures (69). Nanoscale patterning and scanning probe techniques designed to locally pattern the electrical properties of the conducting interface are discussed in the following sections.

4. DEVICE FABRICATION

To realize functional electrical devices in oxide heterostructures, patterning the interfacial 2DEG is necessary. In conventional heterostructures such as GaAs-based quantum wells, the 2DEG is typically buried ∼100 nm below the surface, which places harsh limits on the achievable device feature sizes. However, because in $LaAlO_3/SrTiO_3$ the 2DEG is only nanometers below the surface, the creation of devices with extreme nanoscale dimensions is possible. Here, we overview the main lithographic approaches to patterning $LaAlO_3/SrTiO_3$ down to the nanoscale: conventional lithography with $LaAlO_3$ thickness modulation; ion beam irradiation; and surface modification, including conductive AFM (c-AFM) lithography.

4.1. Lithography and LaAlO₃ Thickness Modulation

Conventional photo- and e-beam-lithographic techniques can be used to laterally define structures by locally controlling the thickness of the crystalline $LaAlO_3$ layer (70) (**Figure 3a**). To ensure that resist residue does not disrupt the conducting interface in the device region, 2 unit cells of $LaAlO_3$ are first deposited epitaxially over the entire substrate (TiO_2-terminated $SrTiO_3$). The sample is next removed from the growth chamber and is patterned with photoresist, after which amorphous $LaAlO_3$ is deposited and the remaining photoresist is lifted off. After this process, the areas that were protected by resist contain pristine crystalline $LaAlO_3$, whereas the other regions are coated
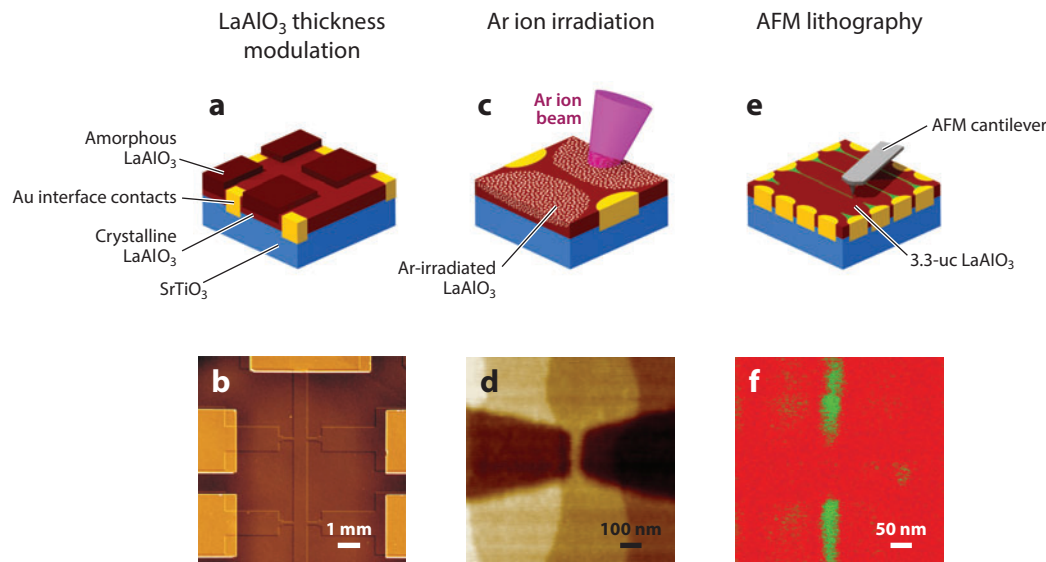
LaAlO₃ thickness
modulation

Ar ion irradiation

AFM lithography

Figure 3

LaAlO$_3$/SrTiO$_3$ device fabrication techniques. Various fabrication techniques are illustrated schematically in panels *a*, *c*, and *e*, whereas the corresponding images of actual devices are shown in panels *b*, *d*, and *f*. (*a*) Conventional lithographic techniques are used to form crystalline LaAlO$_3$ regions with a thickness greater than 3 unit cells (the conducting device region) surrounded by regions with 2 unit cells of crystalline LaAlO$_3$ covered with amorphous LaAlO$_3$ (the insulating region). Feature sizes down to 1 μm with UV photolithography and down to 200 nm with e-beam lithography have been achieved through this technique. (*b*) Optical image of a Hall bar device with 10-μm features fabricated with this approach. Panel *b* adapted with permission from Reference 70. Copyright 2006, AIP Publishing. (*c*) Argon ions can be used to transform conducting LaAlO$_3$/SrTiO$_3$ regions into insulating regions, most likely through the creation of local defects. (*d*) The argon ion technique can produce features as small as 50 nm, as shown by atomic force microscope (AFM) imaging. Panel *d* adapted with permission from Reference 72. Copyright 2013, AIP Publishing. (*e*) A conducting AFM (c-AFM) probe is used to apply voltage to the surface of subcritical-thickness (3.3-unit-cell-thick) LaAlO$_3$, creating locally conducting regions with feature sizes below 10 nm. (*f*) Features created by c-AFM can be imaged through piezoelectric force microscopy. Panel *f* adapted with permission from Reference 77. Copyright 2013, AIP Publishing.

by amorphous LaAlO$_3$. Finally, epitaxial LaAlO$_3$ is grown to a thickness totaling >4 unit cells, defining the conducting regions (regions with amorphous LaAlO$_3$ on top remain insulating). By using this patterning method, conducting features have been made as small as 1 μm with UV lithography and as small as 200 nm with e-beam lithography. A similar e-beam lithography technique using amorphous SrTiO$_3$ as a hard mask prior to growth of epitaxial LaAlO$_3$ was used to fabricate devices as small as 500 nm (71).

4.2. Ion Beam Irradiation

Conducting structures down to 50 nm in size have been fabricated through ion beam irradiation (72) (**Figure 3c**). In this process, a conducting LaAlO$_3$/SrTiO$_3$ (>4-unit-cell) structure is first grown, and e-beam lithography is used to define narrow regions in deposited resist that will ultimately remain conducting. Argon ions are then directed at the sample. After this exposure, regions protected by resist remain conducting, whereas regions exposed to argon ions become insulating, most likely due to the creation of local defects. Ion beams have also been used to modify the interface conductivity without the initial patterning of resist by using a stencil mask (73).

4.3. Conductive Atomic Force Microscope Lithography

Conducting features in LaAlO$_3$/SrTiO$_3$, down to just 2 nm, have been made through the c-AFM technique (74) (**Figure 3e**) to modify the charge state of the top LaAlO$_3$ surface. In doing so, critical-thickness (∼3-unit-cell-thick) LaAlO$_3$/SrTiO$_3$ interfaces can be locally and reversibly switched between conductive phases and insulating phases that are stable for hours in ambient conditions and indefinitely in vacuum or at cryogenic temperatures. The mechanism of formation for this metastable conductive state is the local modification of the surface charge (75) through voltage-mediated addition and removal of water in the form of OH$^-$ and H$^+$ (76). Characterization via piezoforce microscopy (77) (**Figure 3f**) and electric force microscopy (78) of c-AFM-written structures confirms their nanoscale size.

5. TRANSPORT AT THE LaAlO$_3$/SrTiO$_3$ INTERFACE

The ability to confine electrons to a 2D conducting layer in semiconductor heterostructures, mastered over the past four decades, has been a cornerstone in the creation of quantum systems with an extreme degree of tunability and ultrahigh purity. The possibility to engineer analogous structures with transition-metal oxides creates an opportunity for even greater tunability due to the rich physics of the *d*-orbital electrons (79). Oxide-based systems are currently more disordered than III–V semiconductor systems, thus becoming conducting only at carrier densities that are two to three orders of magnitude higher (80) than carrier densities of their semiconducting counterparts. As a result of this high doping, multiple electronic subbands, with carriers of widely different effective masses (light and heavy bands), are expected to be populated within the 2DEG.

5.1. General Transport Phenomenology

To date, transport measurements have been the main approach to studying the properties of LaAlO$_3$/SrTiO$_3$ interfaces (80–94). On the basic level, the angular dependence of the measured magnetotransport has established the 2D nature of the conducting electron system (96). More generally, at high carrier densities (a few 10^{13} cm^{-2}), the transport shows a rather complicated magnetic field dependence, attributed to the occupation of several bands (81–85). Nernst effect measurements (86) have also observed evidence for multiple bands. Several explanations have been proposed to account for the multiband transport and for its characteristic gate voltage dependence. These models have emphasized (*a*) the influence of the confinement potential shape on the distance of the electronic wave functions from the interface, (*b*) the subsequent influence of the corresponding mobilities as set by the gate voltage (81, 87), and (*c*) the effect of terraces in the underlying SrTiO$_3$ substrate (85, 88).

The occupation of many bands might suggest that the transport in LaAlO$_3$/SrTiO$_3$ should be quite complex and strongly dependent on sample-specific details such as disorder, preparation conditions, and LaAlO$_3$ layer thickness. Surprisingly, however, many unique transport phenomena that are unfamiliar in, e.g., III–V-based systems are universally found across LaAlO$_3$/SrTiO$_3$ samples created in various labs throughout the world. In the remainder of this section, we highlight these commonly observed transport features, leaving discussions of superconductivity and magnetism for subsequent sections.

5.2. Anisotropic Magnetoresistance

One of the most surprising observations is the unusual anisotropy of transport at strong magnetic fields. For fields oriented in the plane of the 2DEG, magnetoresistance is large and negative, often showing a dramatic (approximately sixfold) drop in resistance compared with its value at zero field

(89, 90). This negative magnetoresistance is very sensitive to the angle of the applied field and disappears when the field is tilted slightly out of the plane (~1°; see **Figure 4a**, lower panel). Furthermore, there is a strong anisotropy in transport with respect to the angle of the applied field within the plane of the 2DEG (**Figure 4a**, upper panel) (89). At very low temperatures, Shubnikov–de Haas oscillations in the longitudinal resistivity have also been observed (82, 83), reflecting a carrier density that is an order of magnitude lower than that measured by the Hall effect, a discrepancy that has so far eluded a clear explanation. At small perpendicular fields, the magnetoresistance changes sign as a function of gate voltage from negative (weak localization) to positive (weak antilocalization) (91, 92) (**Figure 4b**). The latter is interpreted as arising from spin-orbit coupling with a rather large energy scale (~10 meV) that is comparable to the Fermi level of the system. Curiously, the onset of spin-orbit effects (91, 93) occurs suddenly at a certain carrier density and correlates well with the emergence of superconductivity.

5.3. A Universal Lifshitz Transition from Single-Band to Multiband Transport

At sufficiently low carrier densities in high-mobility samples, a simpler, more general view of transport begins to emerge. Experiments have shown (94) that in these samples there is a critical carrier density below which the transport follows a simple single-band behavior, which is evident from a Hall voltage that is linear in field. Above this density, a transition to nonlinear Hall curves occurs, which is consistent with two-band transport (**Figure 4c**). Curiously, this transition occurs at a universal critical density of $\sim 1.7 \times 10^{13}$ cm^{-2} across a broad range of sample mobilities and LaAlO$_3$ thicknesses (94). This universality suggests that the observed transition is different from a disorder-driven metal-insulator transition (80) and that it instead originates from the intrinsic properties of the 2DEG.

The emerging picture is that the critical density corresponds to a Lifshitz transition between (*a*) the population of only a single, light, circular d_{XY} band and (*b*) the additional population of two heavy d_{XZ} and d_{YZ} bands (**Figure 4d**). Gate-dependent angle-resolved photoemission spectroscopy (ARPES) measurements recently confirmed this simple view (97). The sudden appearance of spin-orbit interactions as a function of gate voltage naturally follows from this band picture because atomic spin-orbit interactions should be most prominent where bands are degenerate, which is precisely the situation of the heavy bands at the Lifshitz transition. Because the Rashba spin-orbit coupling is proportional to the atomic spin-orbit coupling, its influence is also peaked at the Lifshitz transition. The resulting band structure (**Figure 4d**) was introduced in Reference 94, was described in terms of microscopic system parameters (11, 95), and was used to explain various magnetotransport phenomena in LaAlO$_3$/SrTiO$_3$ (92, 98, 99).

Although the understanding of the basic elements of LaAlO$_3$/SrTiO$_3$ transport is beginning to coalesce, many important topics remain unresolved and not fully explored. Of particular note are the influence of disorder and sample inhomogeneities; the lifting of orbital degeneracies by the various symmetry breakings occurring in SrTiO$_3$, e.g., through local lattice distortions that lead to channeled flow, as discussed in Section 8 (3, 4); and how these factors can be controlled on the nanoscale with an eye toward novel device applications.

6. SUPERCONDUCTIVITY

SrTiO$_3$ is the most dilute superconductor found in nature (100) and was the inspiration for Bednorz & Müller (101) in their quest for high-temperature superconductors. Bulk SrTiO$_3$ becomes a superconductor (18, 102) at sufficiently high doping ($\sim 5 \times 10^{17}$ cm^{-3}) and at sufficiently low temperatures (critical temperature $T_c \sim 300$ mK). The superconducting critical temperature has a dome structure as a function of the 3D carrier density (102) (**Figure 1d**), reaching a maximum
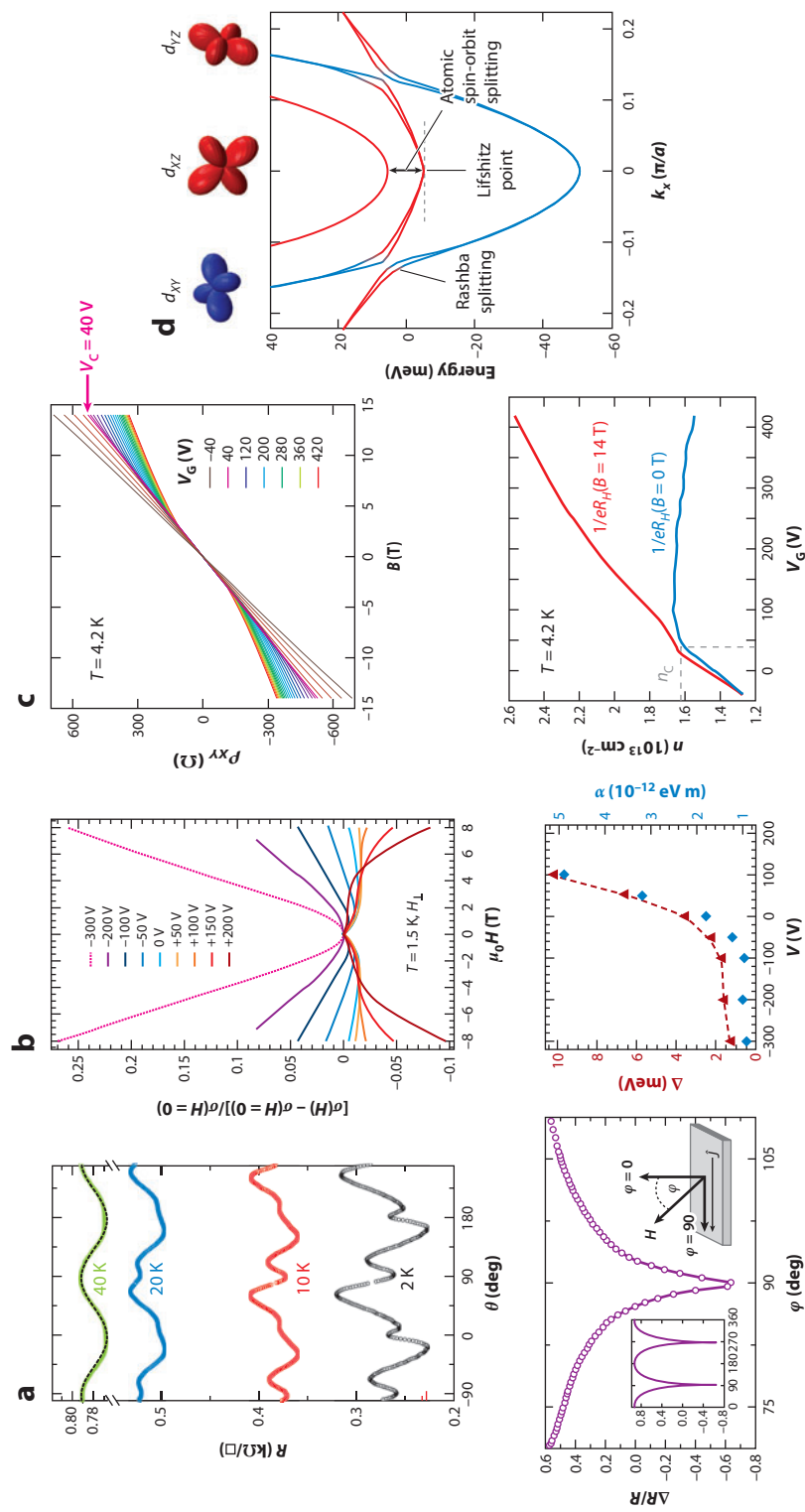
Figure 4

Transport at the LaAlO₃/SrTiO₃ interface. (*a*) Magnetoresistance anisotropy. Strong, negative magnetoresistance is observed when the magnetic field is parallel to the interface, disappearing sharply as the magnetic field is tilted out of the plane (*lower panel*). Strong anisotropies are also observed as a function of the angle of the field in the plane with respect to the direction of current (*upper panel*). Panel *a* reprinted with permission from Reference 89. Copyright 2009, the American Physical Society. (*b*) Spin-orbit coupling. Conductance shift as a function of perpendicular field changes sign as the gate voltage is made more positive (*upper panel*), from weak localization to weak antilocalization, indicating an abrupt onset of strong spin-orbit coupling, with a characteristic scale reaching ~10 meV (*lower panel*). Panel *b* reprinted with permission from Reference 91. Copyright 2010, the American Physical Society. (*c*) Lifshitz transition at a universal critical density. For high-mobility samples, a transition from linear Hall curves occurs as the gate voltage is swept, signifying a transition from single- to two-band transport (*upper panel*). This transition occurs at a universal critical density of ~1.7 × 10¹³ cm⁻² independently of electronic mobility and LaAlO₃ thickness. This critical density corresponds to a Lifshitz transition (*lower panel*), below which only a single, light band (*d_XY*) is occupied and above which two additional heavy bands (*d_YZ* and *d_XZ*) are populated. Panel *c* adapted with permission from Reference 94. Copyright 2012, Macmillan Publishers. (*d*) Band structure (along the *k_XY* direction) that captures the various magnetotransport phenomena. Color-coded subbands represent bands formed from the corresponding *d* orbitals shown above.

$T_c \sim 300$ mK for densities of $\sim 10^{20}$ cm^{-3}. Although superconductivity in SrTiO$_3$ is generally believed to be described by the Bardeen-Cooper-Schrieffer (BCS) theory of superconductivity (103, 104), there is still an ongoing debate as to whether Cooper pairing is simply phonon mediated or unconventional. A number of energy bands contribute to the superconducting state (105, 106), and spin-orbit interactions and FM can lead to other exotic pairing mechanisms such as a Fulde-Ferrell-Larkin-Ovchinnikov (FFLO) state (107–109).

6.1. Superconducting Phase Diagram

The 2DEG in LaAlO$_3$/SrTiO$_3$ heterostructures also becomes superconducting at sufficiently low temperatures (110), with features that are strongly reminiscent of bulk SrTiO$_3$ superconductivity. Again, a characteristic superconducting dome has been observed as a function of carrier density (111) (**Figure 5a**), with a maximum $T_c \sim 300$ mK, which is close in value to that observed in the bulk. Due to this high degree of similarity with bulk superconductivity, the superconductivity in LaAlO$_3$/SrTiO$_3$ may be understood by considering the effective 3D density that corresponds to the electrons localized near the interface. In contrast, the superconducting dome also bears strong resemblance to the dome structure seen in high-T_c superconductors (**Figure 5b**), and recent tunneling measurements even observed the existence of a pseudogap in LaAlO$_3$/SrTiO$_3$ with a carrier dependence similar to that observed in high-T_c superconductors (112), suggesting that this feature may be endemic to 2D superconductivity.

6.2. Local Structure of Superconductivity

Scanning SQUID (superconducting quantum interference device) measurements have provided insights into the structure of superconductivity on microscopic scales (21). These studies have
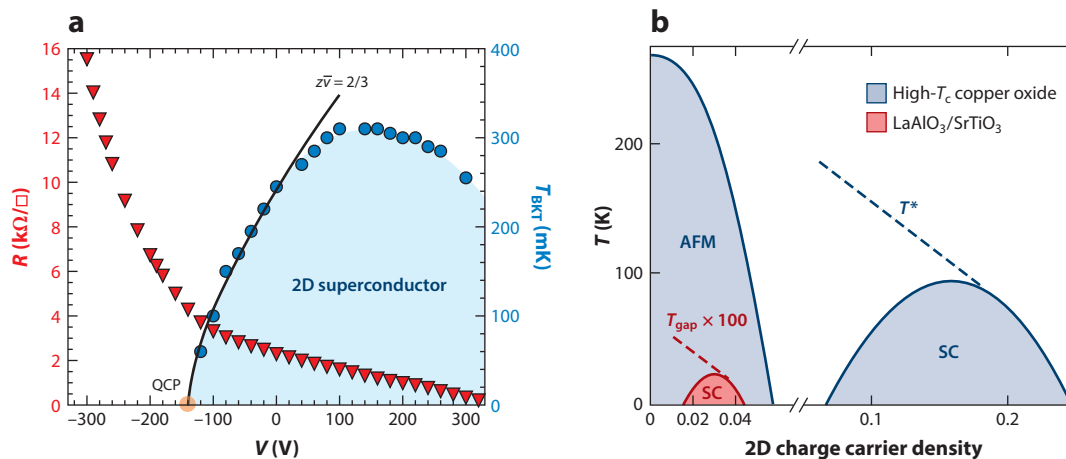

Figure 5

Superconductivity. (*a*) Superconducting critical temperature of LaAlO$_3$/SrTiO$_3$ (*blue circles*) and normal-state sheet resistance (*red triangles*) measured as a function of gate voltage. The superconductivity has a clear dome structure. Panel *a* adapted with permission from Reference 111. Copyright 2008, Macmillan Publishers. (*b*) Illustration of data from LaAlO$_3$/SrTiO$_3$ tunneling measurements that identify a characteristic line above the critical temperature at which a pseudogap opens (*dashed red line*). This state is strongly reminiscent of the pseudogap state in high-T_c superconductors (drawn to scale in *blue*). Panel *b* adapted with permission from Reference 112. Copyright 2013, Macmillan Publishers. Abbreviations: AFM, antiferromagnetic; QCP, quantum critical point; SC, superconducting; T^*, pseudogap temperature; T_{BKT}, Berezinskii-Kosterlitz-Thouless (BKT) critical temperature; T_{gap}, LaAlO$_3$/SrTiO$_3$ gap closing temperature.

shown that in LaAlO$_3$/SrTiO$_3$ superconductivity is spatially inhomogeneous, in contrast to superconductivity in delta-doped SrTiO$_3$. Additionally, the superfluid density in LaAlO$_3$/SrTiO$_3$ is tunable with gate voltage (113) and quite small in magnitude (a few 10^{12} cm^{-2}) (111), ten times lower than the total carrier density measured via the Hall effect. Gate voltage dependence studies have also revealed a correlation between the peak of the superconducting dome and the Lifshitz transition between light and heavy subbands (94), emphasizing the possible importance of the different subband symmetries in the formation of the superconducting ground state.

6.3. Superconductivity and Magnetic Fields

Measurements of the superconducting critical magnetic field, H_c, demonstrate strong anisotropies for fields applied in and out of plane. Such anisotropy confirms that the superconductivity is 2D in nature, placing an upper bound of 10–50 nm on the thickness of the superconducting layer (93, 114). Measurements of the critical perpendicular field, analyzed within the Ginzburg-Landau theory, give an estimated coherence length of ~50–100 nm. The critical in-plane field is curiously observed to be substantially (up to 4 times) larger than the Chandrasekhar-Clogston limit, according to which the conventional superconducting singlet is destroyed once the applied field is strong enough to align in parallel the two constituent spins; i.e., $g\mu_B B \sim \Delta$, where g is the Landé g-factor, μ_B is the Bohr magneton, B is the magnitude of the in-plane field, and Δ is the superconducting energy gap. In-plane fields can even be exploited to increase the critical superconducting temperature (115). These observations highlight the strong effects of spin-orbit interactions and suggest that an unconventional form of superconducting pairing may be at play.

Remarkably, as is more fully discussed in the following section, superconductivity in LaAlO$_3$/SrTiO$_3$ is often observed to coexist with magnetism within the same sample (21). These phenomena are generally considered to be mutually exclusive, and it is not yet clear whether they occur in regions of the sample separated in space or whether they occur within the same region, in which case the superconductivity would be of an unconventional form possibly involving spin-orbit coupling (109, 116). Future investigations with nanoscale probes are necessary to resolve this issue. Recent application of AFM-based techniques has even resulted in superconductivity in quasi-1D nanoscale structures (117). These observations pave the way to controlling superconductivity over nanometer length scales.

7. MAGNETISM

The existence of magnetism at the LaAlO$_3$/SrTiO$_3$ interface is perhaps one of the most surprising and least understood phenomena in this system. Although neither of the parent compounds (SrTiO$_3$ and LaAlO$_3$) is magnetic, after an interface between them is formed, clear signatures of magnetic order emerge and often persist up to room temperature. In this section, we review the understanding gained by recent experimental and theoretical works on magnetism in LaAlO$_3$/SrTiO$_3$ and address the following fundamental open questions: Is the magnetism attributable to localized electrons, itinerant electrons, or a combination of both? What are the magnetic ground states of the system? Can these magnetic states be tuned with gate voltage as can the electrical and mechanical properties of this interface?

7.1. Experimental Manifestations of Magnetism at the LaAlO$_3$/SrTiO$_3$ Interface

So far, experiments have uncovered two manifestations of magnetism. The first is FM, which is typically observed at low magnetic fields, involves a large number of spins, occurs in inhomogeneous

patches that vary strongly between and within samples, and shows no gate voltage dependence. The second is seen via magnetoresistance measurements and points to a gate voltage–dependent metamagnetic transition (a rapid increase in magnetism at a finite applied magnetic field) that strongly involves the conduction electrons. We discuss both of these manifestations below.

Indications of magnetism in $LaAlO_3/SrTiO_3$ were first uncovered (19) through low-temperature (300-mK) measurements of 2DEG resistance that showed clear signs of magnetoresistance (**Figure 6a**), hinting at the existence of a field-switchable, spontaneous magnetization. Soon thereafter, FM hysteresis was demonstrated up to room temperature and was shown to coexist with paramagnetic and diamagnetic susceptibilities (22), suggesting that the electrons have multiple coexisting phases. Similar hysteresis observed in the superconducting critical current (23) signified that the coexistence is with superconductivity. The existence of FM was further corroborated by torque magnetometry (24), which measured the magnetization of $LaAlO_3/SrTiO_3$ directly and showed that it is large, even within the superconducting state (**Figure 6b**). Scanning SQUID experiments elucidated the microscopic nature of this coexistence (21). These studies revealed that FM is concentrated in sparse random patches, each having a large magnetic dipole surrounded by a majority of non-FM superconducting regions (**Figure 6c**). To date, it is not known whether FM and superconductivity (or even normal conductivity) occur in the same regions within a sample, in different layers, or side by side. Within the FM patches, the magnetic moments are aligned in plane, and their density is quite high (a few 10^{14} cm^{-2}) (21, 25). However, as these patches are sparsely distributed, the overall interfacial moment density is rather low (a few 10^{12} cm^{-2}) (21, 25). Such low density is consistent with measurements by various macroscopic probes (26–28), with the exception of torque magnetometry experiments (24), which observed a moment density approaching the limit of half an electron per unit cell over the entire sample. X-ray circular dichroism revealed that the moments contributing to the FM arise from localized d_{XY} states of titanium atoms, which lie very close to the interface, most probably within the first TiO layer (28).

7.2. Origin of Ferromagnetic Moments

Two fundamentally different scenarios are proposed for the emergence of FM moments in $LaAlO_3/SrTiO_3$. The first scenario (**Figure 6g**, upper panel) attributes such moments to the intrinsic instability of a special d_{XY} energy band, which is theoretically predicted to split off to lower energies and to be much more localized than the other interfacial bands such that it resides only in the first TiO plane adjacent to the interface (29). This band is expected to accommodate the majority of carriers transferred to the interface, which within the polarization catastrophe hypothesis is predicted to reach half an electron per titanium atom for thick $LaAlO_3$. Such a high carrier population effectively makes this band a quarter-filled Mott insulator, driving carriers to localize on every second titanium site such that they do not participate in conduction, thereby explaining why only a small fraction of the total charge density is actually measured in transport. These localized carriers are extremely susceptible to magnetic polarization either through a Stoner-like mechanism (29) or through interactions with a small fraction of conduction electrons (109). The experimental observation (25) that FM emerges only above a critical $LaAlO_3$ thickness that is nearly equal to that in which the 2DEG conductivity emerges would be consistent with this scenario.

A second scenario (**Figure 6g**, lower panel) relates the FM moments to an extrinsic source. The observation of randomly distributed FM patches within a sample (21), the large variability between samples (21, 25), the high sensitivity to strain (30), the lack of gate voltage dependence (25, 113), and the observed dependence on the oxygen growth pressure (19, 22) make oxygen vacancies
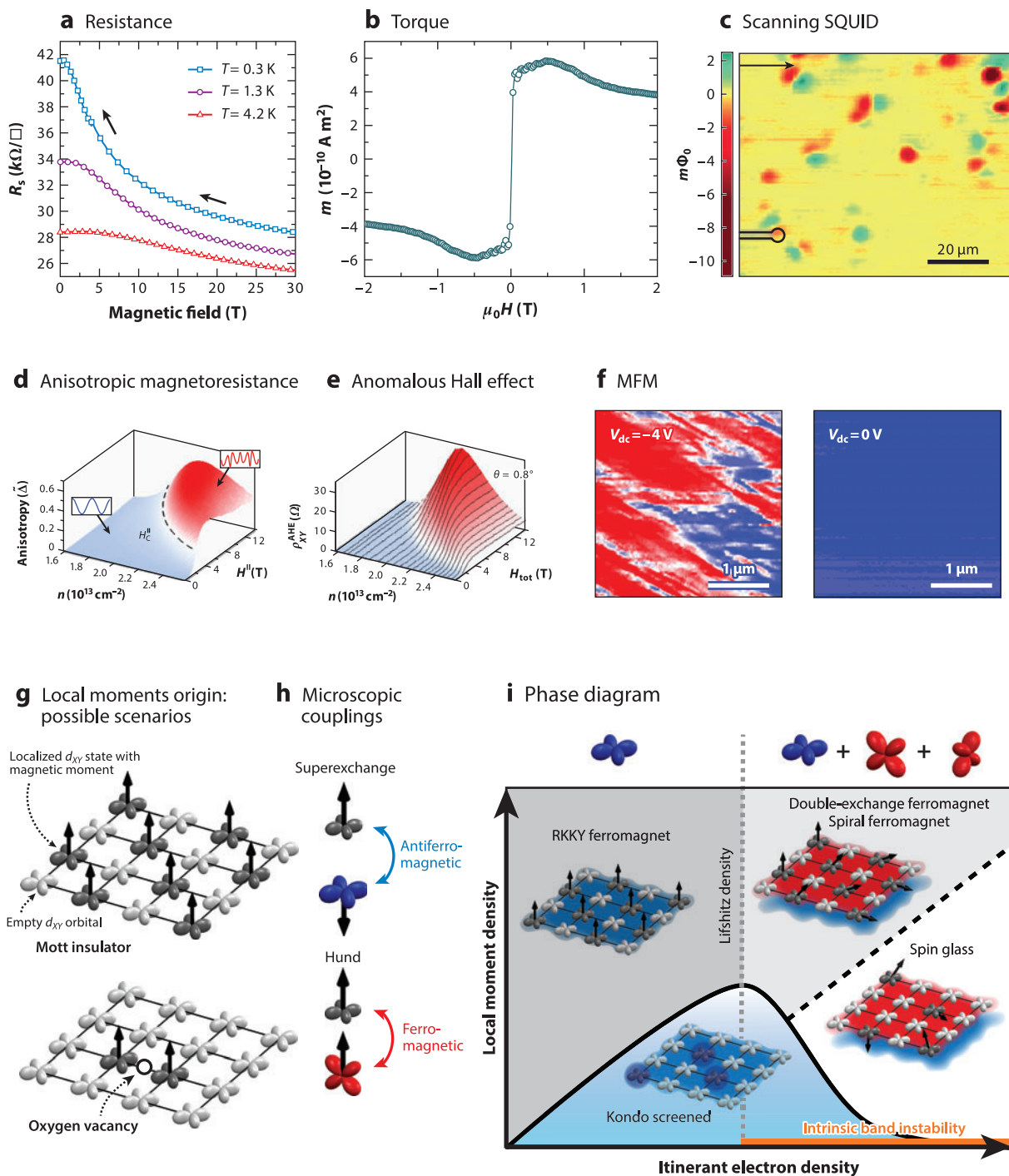
and their possible aggregation within the sample a prime suspect. Indeed, density functional theory calculations show that titanium atoms around an oxygen vacancy should develop a large local magnetic moment (31). In contrast to the intrinsic scenario above, here the density of free moments is highly variable and dependent on the details of sample preparation.

In those samples that contain FM patches, the magnetization within the patches is quite large. One may wonder whether in these samples magnetism also exists within the majority of 2DEGs outside of these patches or even in samples that do not contain patches. A much smaller but still nonzero density of moments is expected to exist in these regions, which may have a density comparable to that of the conduction electrons. In this regime, the interaction between these dilute moments and conduction electrons may give rise to interesting magnetic ground states in which these two components are players on an equal footing.

Magnetotransport experiments provided evidence for such magnetic ground states that strongly depend on the density of the itinerant electrons (32). These experiments suggest the existence of a metamagnetic transition beyond a critical magnetic field (see Section 5). Around this field, dramatic changes are observed in the ground state of the system: Below the critical field, the magnetoresistance is isotropic in the plane of the interface, but directly above this field it becomes strongly anisotropic ($\sim$50%), with preferred axes along crystalline directions (32, 33) (**Figure 6d**). Concurrent with these observations is a strong, anomalous Hall effect component that emerges when the critical field is crossed and that saturates soon thereafter (32, 34), indicating a sudden buildup of internal magnetization (**Figure 6e**). Finally, the longitudinal resistance drops dramatically above the critical field and saturates on a value that is smaller by almost an order of magnitude (32, 33, 89). These three effects occur in perfect synchrony and are suggestive of a metamagnetic transition between a nonmagnetic phase below the critical field and a polarized magnetic phase with preferred easy axes above it; the latter phase is similar to that observed in dilute magnetic semiconductors (118, 119). The metamagnetic critical field depends strongly on gate voltage, with its value smoothly increasing with decreasing carrier density and appearing to diverge as the Lifshitz point is approached from above (at the bottom of the heavy d_{XZ}/d_{YZ} bands). This dependence indicates that the conduction electrons play a central role in the observed magnetic phases. The correlation between the divergence of the critical field and the Lifshitz point, which corresponds to the transition between solely populating the d_{XY} band and additionally populating the d_{XZ}/d_{YZ} bands, signifies that the orbital symmetry of the conducting electrons also has an important effect on the resulting magnetic ground states. Gate-tunable magnetic states have further been observed at the low-density side of the phase diagram. Magnetic force microscope measurements revealed (35) (**Figure 6f**) that as the conduction electrons are depleted, the interface becomes FM even at room temperature, with a domain structure on the micrometer scale. Unlike the FM discussed above, here the FM disappears completely as the conduction electrons are populated under the application of a gate voltage.

7.3. Magnetic Phase Diagram

Several theoretical works studied the different magnetic phases that may appear at the LaAlO$_3$/SrTiO$_3$ interface. All these works can be cast into a generic phase diagram describing the magnetic order as a function of the itinerant carrier density and the local moment density (**Figure 6i**). One class of theories (92, 99, 120) assumed that impurities are irrelevant, explaining the observed magnetic order as an intrinsic Stoner-like instability of the itinerant d-bands. Such an instability may occur near the Lifshitz point, where the strong spin-orbit interactions that exist as the two heavy d_{XZ}/d_{YZ} bands become populated may greatly enhance the density of states. Other theories (32, 109, 116, 121–123) emphasized the crucial role played by localized moments and

a Resistance

b Torque

c Scanning SQUID

d Anisotropic magnetoresistance

e Anomalous Hall effect

f MFM

g Local moments origin: possible scenarios

h Microscopic couplings

i Phase diagram

their coupling to the itinerant electrons in determining the magnetic ground states. Two opposite microscopic couplings between localized electrons and itinerant electrons follow directly from the symmetries of the underlying orbitals (**Figure 6b**). Both localized electrons and itinerant electrons originate from the titanium d orbitals; the former electrons populate only d_{XY} states, and the latter electrons populate d_{XY} states below the Lifshitz transition and additional d_{XZ}/d_{YZ} states above this transition. Due to Pauli exclusion, an itinerant d_{XY} electron can hop onto a titanium site that is occupied by a localized d_{XY} moment only if it has the opposite spin, leading to antiferromagnetic coupling (superexchange). Itinerant d_{XZ}/d_{YZ} electrons, in contrast, do not have this limitation and thus have FM Hund's coupling to the local moments. The magnetic order depends on the relative density of localized moments and itinerant electrons and on the orbital nature of the itinerant electrons. If d_{XY} itinerant electrons are occupied and their density is much lower than that of the localized moments, they induce RKKY interactions that ferromagnetically align the moments (109). Dilute, itinerant d_{XZ}/d_{YZ} electrons also induce FM order, but through a double-exchange mechanism (124, 125) that is driven by Hund's rule–induced alignment of itinerant electron spins and by the spin of the localized moments. Due to this alignment, the itinerant electrons can hop most easily between localized sites whose spins are ferromagnetically aligned, and the resulting gain in kinetic energy leads to an effective FM interaction between the localized moments. If Rashba spin-orbit interactions are also present, the spin of the itinerant electrons rotates as they hop between sites, stabilizing a spin spiral ground state (121). One can show through general symmetry arguments that skyrmions and cone states may also be a stable ground state (123).

Further interesting phases may be found when the density of local moments becomes comparable to the itinerant electron density. Antiferromagnetic coupling to itinerant d_{XY} electrons leads to a nonmagnetic Kondo-screened phase (19, 32, 122). However, once the d_{XZ}/d_{YZ} electrons, which have competing FM interactions with the moments, begin to accumulate, the Kondo phase starts to diminish. As a result, the corresponding Kondo temperature decreases with increasing carrier density (32, 122). This scenario is so far the only model that can explain the experimentally observed reduction of the metamagnetic critical field with increasing carrier density. At still higher

←——

Figure 6

Magnetism (*a–f*) Various measurements of magnetism at the LaAlO$_3$/SrTiO$_3$ interface reveal a rich phenomenology. (*a*) Magnetoresistance in perpendicular field. Panel *a* adapted with permission from Reference 19. Copyright 2007, Macmillan Publishers. (*b*) Large in-plane magnetization measured by torque magnetometry. Panel *b* adapted with permission from Reference 24. Copyright 2011, Macmillan Publishers. (*c*) Magnetic dipoles imaged with scanning SQUID microscopy. Panel *c* adapted with permission from Reference 21. Copyright 2011, Macmillan Publishers. (*d*) A gate-tunable metamagnetic transition between phases with weak (*blue*) and strong (*red*) magnetoresistance anisotropy. Panel *d* from Reference 32. (*e*) Emergence of an anomalous Hall effect corresponding to the metamagnetic transition in panel *d*. Panel *e* from Reference 32. (*f*) Room-temperature ferromagnetism measured via magnetic force microscopy (MFM). Panel *f* from Reference 35. (*g*) The two proposed scenarios for the emergence of local magnetic moments in LaAlO$_3$/SrTiO$_3$. (*Top panel*) A Mott insulator formed from a quarter-filled ($1/2e^-$ per unit cell) d_{XY} energy band, localized in the first TiO plane of SrTiO$_3$ near the interface. The lattice sites correspond to the Ti atoms in this plane. The white orbitals represent empty states, whereas the gray orbitals represent localized d_{XY} states, and the black arrows represent their local magnetic moments. (*Bottom panel*) An alternative scenario in which the magnetic moments arise near oxygen vacancies. (*h*) Microscopic couplings between itinerant and localized moments. An effective antiferromagnetic (superexchange) interaction due to Pauli exclusion couples itinerant d_{XY} electrons (*blue*) to localized d_{XY} moments (*gray*). Conversely, for itinerant d_{YZ} and d_{XZ} electrons (*red*), hopping is allowed for both spin orientations, resulting in a ferromagnetic Hund's coupling to the localized d_{XY} moments (*black*). (*i*) The emerging phase diagram, showing the magnetic phases formed in the plane parameterized by itinerant electron density and local moment density: RKKY ferromagnet (109), double-exchange ferromagnet (116, 121) or spiral (121, 123), spin-glass state (122), Kondo-screened phase (19, 32, 122). Relevant itinerant orbitals for different density regimes are shown above the diagram. The critical Lifshitz density (*dashed vertical line*) indicates the density above which itinerant d_{YZ} and d_{XZ} electrons are populated. Intrinsic band stability scenarios (92, 99, 120) are shown by the orange-shaded region.
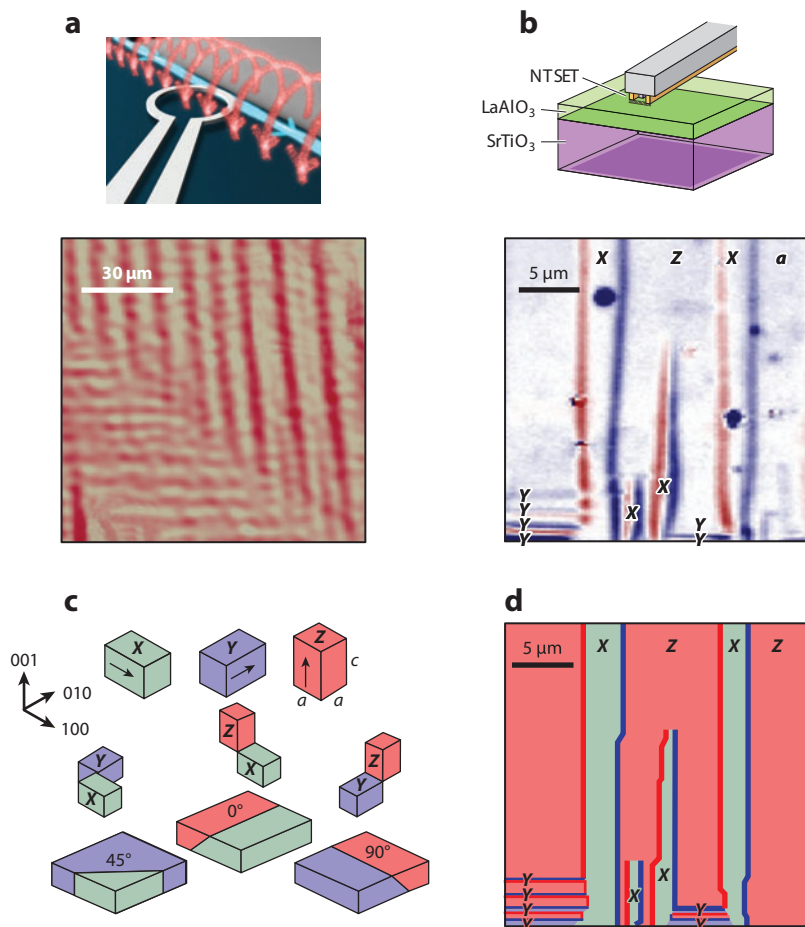
Figure 7

Ferroelasticity. (*a*) (*Upper panel*) Illustration of a scanning SQUID probe used for imaging current flow.
Magnetic field lines (*red*) generated by a current path (*blue*) thread the SQUID loop. (*Lower panel*) An image
of current flow through the LaAlO$_3$/SrTiO$_3$ interface captured with such a scanning SQUID probe. Red
indicates high current density, whereas white indicates low current density. Strikingly, the current flows in
narrow channels. Panel *a* reprinted with permission from Beena Kalisky. (*b*) Scanning nanotube-based
single-electron transistor (NT SET) imaging. The upper panel shows a NT SET probe hovering above the
surface of an LaAlO$_3$/SrTiO$_3$ sample. By scanning of this SET across the LaAlO$_3$/SrTiO$_3$ surface, the local
electrostatic landscape can be imaged. The lower panel shows an image taken via scanning SET of gate
voltage–induced domain wall motion in LaAlO$_3$/SrTiO$_3$. The image contains various patterns of stripes;
each stripe represents the motion of either the rising edge (*red*) or the falling edge (*blue*) of a potential step in
the surface induced by an oscillating back-gate voltage. Panel *b* adapted with permission from Reference 4.
Copyright 2013, Macmillan Publishers. (*c*) Tetragonal domain tiling rules. Below the ferroelastic transition,
the cubic SrTiO$_3$ unit cells distort into elongated rectangular prisms, forming domains characterized by the
orientation of their long *c*-axes, which may lie along the *X* (*green*), *Y* (*blue*), or *Z* (*red*) direction. Intersections
of different domain orientations must share their short *a*-axis to minimize dislocations, forming twin
boundaries with characteristic angles of either 0°, 45°, or 90° with respect to the crystallographic axes as
viewed from above. Panel *c* adapted with permission from Reference 4. Copyright 2013, Macmillan
Publishers. (*d*) Schematic map labeling the domain orientations imaged in panel *b*. The dark red and blue
lines represent the domain wall boundaries. The coloring of the domains is the same as in panel *c*.

carrier densities, the random sign of the RKKY interactions mediated by the itinerant electrons leads to a spin-glass state (122).

Although a clarified, coherent view of magnetism at the $LaAlO_3/SrTiO_3$ interface is emerging, there are more open questions than answers. Local magnetic structure, coupling to the electronic degrees of freedom, and the possibility for magnetism at ferroelastic domain walls are areas that require further investigation. Ultimately, as our understanding of magnetism in the oxides further crystallizes, we may hope to exploit the gate-tunable phase diagram to control magnetic structures and interactions at the nanoscale.

8. FERROELASTICITY: THE MICROSCOPIC STRUCTURE OF DOMAINS

Until recently, studies on complex oxide heterostructures focused primarily on the electrical and magnetic properties of the conducting interface, neglecting the influence of the rich structural phenomenology of the $SrTiO_3$ substrate, in particular its ferroelasticity. The primary reason that experimental progress has been hindered is that standard surface science probes such as STM are insufficient for studying the buried interfaces presented by oxide heterostructures. In this section, after first extending the discussion of ferroelasticity in $SrTiO_3$, we describe the results of experiments employing novel nanoscale probes to study the ferroelastic state in $SrTiO_3$ and its important influence on the $LaAlO_3/SrTiO_3$ interface.

8.1. Ferroelastic Domains in $SrTiO_3$

The ferroelastic state of $SrTiO_3$ emerges below $T = 105$ K and is characterized by the breaking of the cubic point-group symmetry of the unit cell (7, 8, 126). Below this transition temperature, the crystal unit cells become rectangular prisms whose long axes may be oriented along any of the crystal axes (X, Y, or Z) (**Figure 7c**). By analogy with FM or ferroelectricity, the transition to the ferroelastic state is accompanied by the formation of domains characterized by the orientation of their unit cells, which distribute to minimize the built-in strain profile in bulk $SrTiO_3$. These domains obey a simple set of tiling rules: To minimize dislocations, unit cells in neighboring domains with orthogonally elongated unit cells must share their a-axes at domain walls (twin boundaries). The resulting domain wall patterns are outlined in **Figure 7c**. Such ferroelastic domain wall patterns were observed in bulk $SrTiO_3$ via polarized optical microscopy more than half a century ago (9, 10).

8.2. Domain Structure and Influence on Transport

With the advent of novel probes suited for studying buried interfaces, experiments are now revealing the important consequences of the ferroelastic domain structure for the 2DEG at the interface between $LaAlO_3$ and $SrTiO_3$. Advances in scanning single-electron transistors (SETs) now allow for noninvasive imaging of the local mechanical response and electrostatic landscape in these buried interfaces with unprecedented sensitivity by using a nanotube quantum dot as a charge detector placed at the end of a scanned-probe cantilever (4) (**Figure 7b**, upper panel). Recent scanning SET studies of $LaAlO_3/SrTiO_3$ have uncovered that an applied back-gate voltage couples to the domains, possibly through anisotropic electrostriction (127) or through charged/polar domain walls (128–130), and can readily move the domain walls. This gate voltage–induced domain wall motion leads to an anomalously large piezoresponse in $SrTiO_3$ (4, 131). By taking into account the above-mentioned tiling rules, these measurements of the local electromechanical response (**Figure 7b**, lower panel) even allow for the specific labeling (**Figure 7d**) of the domain orientations as viewed from above the $LaAlO_3/SrTiO_3$ interface.

Scanning SET measurements have also shown that the ferroelastic domains in $SrTiO_3$ create a varying potential landscape at the $LaAlO_3/SrTiO_3$ interface (4), where the potential differs between regions of in-plane (*X* or *Y*) and out-of-plane (*Z*) domains. To maintain electrochemical equilibrium, charge must transfer between domains of varying potential, creating a dipole-like charge distribution at the domain walls and possibly leading to strong enhancement of charge density in the 2DEG at these walls. As electron mobility is a strong function of carrier density in $LaAlO_3/SrTiO_3$ (132), such charge enhancement may then lead to channeled current flow (133).

Such channeled current flow was recently observed in scanning SQUID measurements (3) (**Figure 7a**). In these measurements, the magnetic field generated by current flow is imaged, and these data are used to generate a spatial map of current density at the $LaAlO_3/SrTiO_3$ interface. By comparing current maps recorded at sample temperatures above and below the ferroelastic transition temperature for $SrTiO_3$, these measurements led to the discovery that current within the 2DEG flows in narrow, parallel channels that arise from the ferroelastic domains in the underlying $SrTiO_3$. On the basis of the cumulative set of scanning data acquired from several different samples, the current likely flows along the domain walls rather than preferentially within the bulk of one domain orientation, although improved experimental resolution is required to directly differentiate between these scenarios. Furthering the understanding of the physics of this channeled flow promises to be a major thrust of future research in the oxide interfaces.

8.3. Toward Domain-Based Nanosystems

As with the other emergent properties of $SrTiO_3$ discussed above, ferroelastic domains increase the complexity of an already very rich class of physical systems, making the interpretation of macroscopic experiments more challenging. However, this new degree of freedom, if controlled and probed on the nanoscale, presents exciting new opportunities for engineering unique low-dimensional nanostructures (134). The domain distribution can be manipulated via applied strain as well as with gate voltages, arming researchers with a new level of experimental control over transport at $LaAlO_3/SrTiO_3$ interfaces. For example, one can envision exploiting the domains to create 1D conducting channels, which inherit all the intriguing properties of the 2DEG discussed above, such as superconductivity, magnetism, and strong spin-orbit coupling. These domain-based nanostructures may be combined with other novel nanoscale patterning techniques, including the AFM-based approaches (74) that are the focus of the next section.

9. FUNCTIONAL DEVICES DOWN TO THE NANOSCALE

Having discussed the novel physical phenomena and relevant nanofabrication techniques of $LaAlO_3/SrTiO_3$, we now survey progress toward creating functional devices from this materials system. In this system, feature sizes range from the microscale to the nanoscale.

9.1. Microscale

By exploiting the unique properties of conducting complex oxide interfaces, one can envision creating oxide-based circuit elements that feature novel switching mechanisms relying on the metal-insulator transition or strong electron interactions. Building on advancements made toward realizing such oxide electronics using zinc- and vanadium-based materials (135, 136), exciting progress has been made in developing $LaAlO_3/SrTiO_3$-based circuits. Capacitors (137) and diodes (138) were among the first functional circuit elements made from $LaAlO_3/SrTiO_3$. More recently, fully integrated circuits were created (**Figure 8a**) from top-gated, microscale $LaAlO_3/SrTiO_3$

a Integrated circuits

b Mesoscopic transport

Optical devices

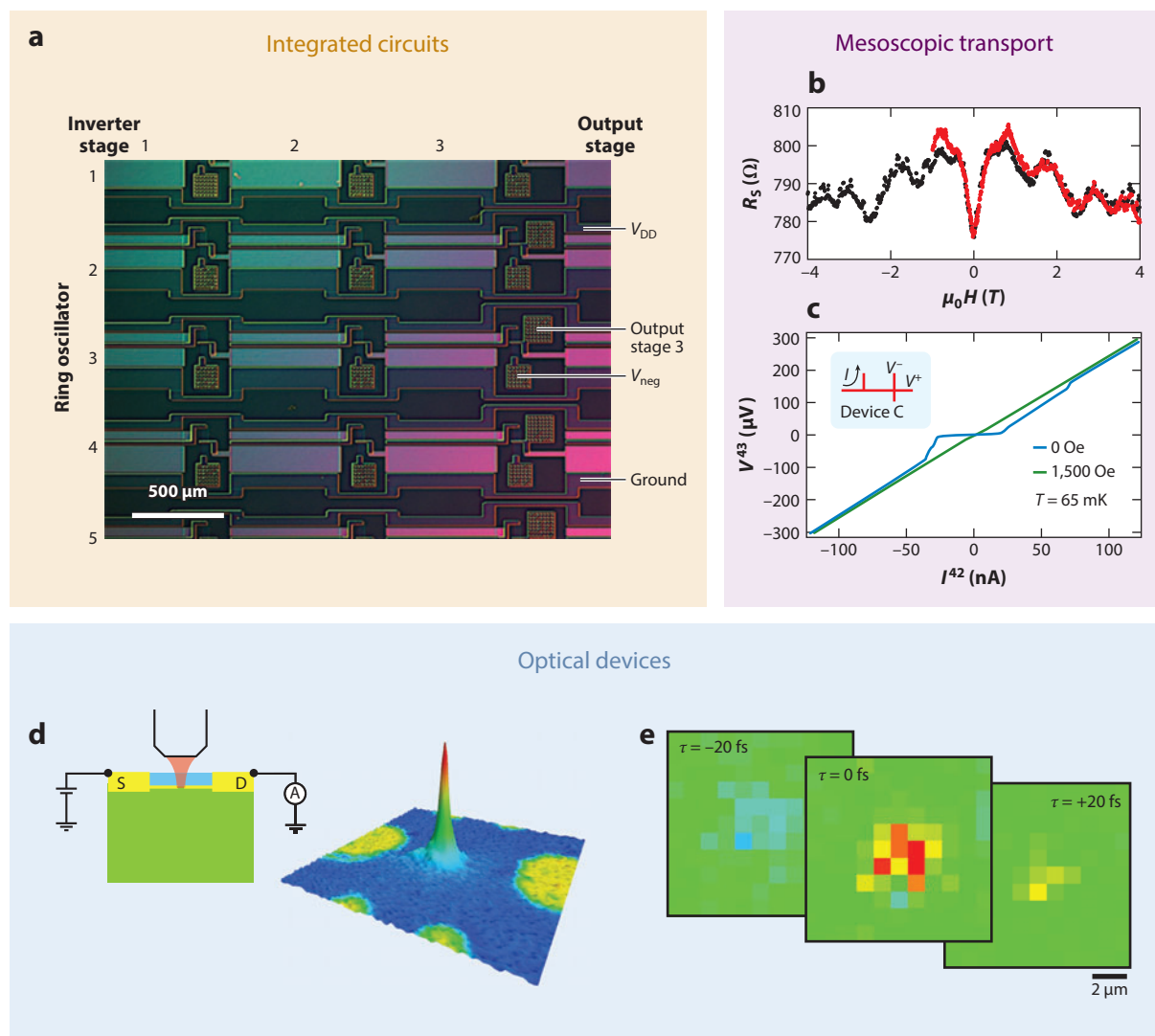**Figure 8**

Functional devices down to the nanoscale. (*a*) Optical microscopy image of a series of ring oscillators made from LaAlO$_3$/SrTiO$_3$, demonstrating the ability to fabricate fully integrated circuits with micrometer-sized features from oxide interfaces. Panel *a* adapted with permission from Reference 139. Copyright 2014, Wiley-VCH. (*b*) Universal conductance fluctuations. Quantum oscillations in conductance as a function of magnetic field are observed in LaAlO$_3$/SrTiO$_3$ devices with dimensions smaller than the phase coherence length. The data shown are from a Hall bar device of size 4 μm × 1.5 μm. The red and black coloring of the data points denotes two separate magnetic field sweeps, highlighting the reproducible pattern of oscillations. Panel *b* adapted with permission from Reference 142. Copyright 2010, the American Physical Society. (*c*) Nonlocal resistance in conducting atomic force microscope (c-AFM)-sketched nanostructures. The inset schematic shows the current path *I* and terminals for voltage measurement V^+ and V^- in a device of length 10 μm and width 10 nm. Cooper pairs form at sufficiently low temperature, blocking spin transport without current flow and thus suppressing nonlocal voltage below the critical current (*blue curve*). Application of an external magnetic field suppresses the superconductivity and restores the nonlocal response (*green curve*). The data shown were taken at $T = 65$ mK. Panel *c* reprinted with permission from Reference 6. Copyright 2013, the American Physical Society. (*d*) Nanoscale devices fabricated by conductive AFM (c-AFM) can be switched optically. (*e*) Ultrafast photoresponse of a c-AFM-sketched LaAlO$_3$/SrTiO$_3$ device with femtosecond dynamics.

field-effect transistors, including arrays of ring oscillators composed of several inverter stages (139). In addition to the active $LaAlO_3/SrTiO_3$ transistors, these devices also featured oxide-based resistors and interconnects, demonstrating the potential for all-oxide circuitry. Increasing the complexity and further miniaturizing these circuits promise to be an important continued research direction.

9.2. Mesoscale

An important series of developments toward the creation of functional $LaAlO_3/SrTiO_3$ nanodevices is the realization of mesoscale devices. For these devices, the physical size of the device influences the electronic properties due to the onset of quantum effects. One indication of such mesoscopic transport is the appearance of universal conductance fluctuations (UCFs) (140, 141), which are signified by fluctuations in conductance on the order of e^2/h, the quantum of conductance. UCFs were observed in $LaAlO_3/SrTiO_3$ samples (**Figure 8***b*), which were small enough with respect to the electrons' phase coherence length to avoid averaging away these quantum oscillations (142). Lithographically defined structures with channels as narrow as 500 nm have exhibited, in addition to UCFs, superconductivity (71), which may be more sensitive to fabrication imperfections, indicating that such fabrication techniques do not deteriorate device quality. In micrometer-scale devices fabricated by reactive-ion etching of $LaAlO_3$, an anomalously large capacitive gating effect with a strong dependence on device size has been observed (143), demonstrating that new and useful features can emerge with shrinking size.

9.3. Nanoscale

c-AFM lithography has proven to be a powerful tool in creating nanoscale devices in $LaAlO_3/SrTiO_3$. Devices with rather complicated geometries can be made by directly writing their pattern with the c-AFM tip. The simplest devices made are nanowires, which, as their width is decreased, give room-temperature resistances of $\sim$100 kΩ/μm and can reach an anomalously high room-temperature mobility of $\sim$400 cm^2/(V $\cdot$ s) (144), rivaling the best silicon-based nanowires. By ramping the voltage applied to the c-AFM tip while moving the tip in contact with the $LaAlO_3$ surface, diodes with positive and negative breakdown voltages can be formed (145). This ability to shape the symmetry of the confining potential that defines the nanowire can potentially be used to modulate spin-orbit interactions in space, which is useful for quantum information processing (146). A simple tunnel junction is formed by negatively biasing the c-AFM tip to locally restore the insulating state of the $LaAlO_3/SrTiO_3$ interface. Such a junction has useful device properties, as it has nonlinear *IV* characteristics governed by the activation barrier and by the nanowire resistance (147).

Low-temperature transport properties of $LaAlO_3/SrTiO_3$-based nanowires exhibit many remarkable and unexplained effects. Similar to the case for the 2D interface, nanowires also undergo a superconducting transition below 200 mK (117). Nonlocal transport is observed in both normal (6) and superconducting (148) states (**Figure 8***c*). In the superconducting state, this effect is attributed to charge imbalance (149, 150), whereas in the normal state the situation is less clear. The combination of FM, strong spin-orbit coupling, and quasi-one dimensionality may lead to helical transport (116), an important starting component for creating Majorana fermions (151, 152), although other explanations may be possible.

A more complex, voltage-tunable nanoscale junction can be created by adding a third electrode (153). These devices can be operated as transistors with on/off ratios of up to 10,000 and are functional up to the gigahertz frequency range (154). To date, *p*-type transistors have not yet been produced with this c-AFM technique, preventing the production of complementary metal

oxide semiconductor (CMOS)-like devices. Nevertheless, unipolar architectures of many common circuit elements (e.g., n-type logic) are in principle possible. Transistor-like behavior has even been achieved by using an optical gate (155). These LaAlO$_3$/SrTiO$_3$ photodetector gates can be operated by using ultrafast sources, allowing for the generation and detection of broadband terahertz emission at the nanoscale (156) (**Figure 8*d,e***). This class of devices may find applications in local molecular characterization and sensing.

An interesting extension deeper into the nanoscale regime is the creation of SETs (157). The ability to create nanoscale islands with tunable couplings represents a fundamental scaling limit for solid-state-device fabrication. SETs fabricated from LaAlO$_3$/SrTiO$_3$ using c-AFM can be scaled to less than 2 nm in size, at which they exhibit a ferroelectric-like, bistable state and show Coulomb blockade up to $T = 40$ K (5). As the number of electrons hosted by the SET can be precisely controlled (0, 1, 2, etc. . .), these devices may be potential building blocks for solid-state quantum simulation.

10. FUTURE DIRECTIONS

This review emphasizes the unique advantages of complex oxide interfaces as platforms for exploring highly varied physical phenomena. Within the same interface, one may simultaneously find a rich set of fundamental physics phenomena. However, the high level of disorder present so far in these materials hinders the ability to disentangle and control these various effects independently, thus limiting this system from reaching its full potential.

One clear route for overcoming the disorder is a continued improvement of materials quality. Through the improved design and growth of these interfaces, it should be possible to separately control the different phenomena and ideally switch them at will, for example, with externally applied voltages. Indeed, the materials science mastery of these interfaces is still in its infancy compared with the much-more-mature field of semiconductors. If successfully adopted, many of the techniques used to advance the field of semiconductors—such as the complete separation of dopants from the conducting channel, lattice matching between different materials, strain engineering, and the optimization of MBE growth (158)—could similarly revolutionize the field of oxide heterointerfaces.

10.1. Beating Complexity by Probing on the Nanoscale

In the context of this complex, disordered landscape of coexisting phenomena, there is another approach of using nanoscale probes to circumvent the elements that currently evade control. Nanoscale probes have already shown that, within a single LaAlO$_3$/SrTiO$_3$ sample, different phenomena like ferroelastic domain walls, superconductivity, and FM can coexist on micrometer scales. When probed on macroscopic scales, the underlying physics of these competing phases is washed out by spatial averaging. However, by probing the interfaces on scales smaller than the typical scales over which these phenomena vary, these phenomena can be independently studied. The natural tendency of these different phenomena to coexist can even be exploited to realize novel nanosystems that are presently too difficult to intentionally engineer but can be readily studied with existing nanoscale probes. One such serendipitous arrangement, for example, could be the creation of 1D conducting channels at ferroelastic domain walls.

Furthermore, existing nanoscale probes can measure important physical quantities of oxide interfaces that have so far been inaccessible via macroscopic approaches. Scanning SETs may be used, for example, to spatially map the full subband structure, to directly identify the dopants that give rise to the itinerant electrons, and to study the nature of electron localization at the interface.

Magnetic force microscopes and the new generation of nanoscale scanning SQUIDs (159) could be used to resolve the physics at ferroelastic domain walls. Optical (160) and microwave (161) nanoscale probes that have proved useful in analogous materials systems are likely to also discover new phenomena at these interfaces.

10.2. Hybrid Systems

Although complex oxide heterointerfaces are buried, they are quite close to the surface compared with semiconductor heterostructures. Due to this proximity, one can envision engineering unique couplings between oxide interfaces and other 2D or even 1D materials outside of the complex oxide family, such as MoS_2, FM thin films, high-temperature superconductors, graphene, nanotubes, and nanowires. Functional electronic, magnetic, and structural couplings and direct tunneling may be explored, extending the parameter space within which to search for novel phenomena. Although forecasting what discoveries will come from these hybrid systems is difficult, the high degree of flexibility of these systems makes them a very intriguing future research direction.

10.3. Engineered Physics with *d*-Orbital Electrons on the Nanoscale

Once a higher degree of cleanliness and control within the complex oxides has been achieved, it will be possible to design systems that maximally exploit the rich properties endowed by the *d*-orbital electrons in the oxides. Independent control over the constituent properties will make the oxide interfaces a powerful laboratory for engineering correlated electron physics on the nanoscale in new, previously inaccessible parameter regimes, including Kondo lattices, engineered Mott insulators, unconventional realizations of the quantum Hall effect, superconductivity in 1D channels, and Majorana fermion states. As both materials quality and the capabilities of nanoscale probes continue to advance, we foresee that the years ahead will be quite exciting for researchers in the field of complex oxide heterostructures.

DISCLOSURE STATEMENT

The authors are not aware of any affiliations, memberships, funding, or financial holdings that might be perceived as affecting the objectivity of this review.

ACKNOWLEDGMENTS

LITERATURE CITED

1. Ohtomo A, Hwang HY. 2004. A high-mobility electron gas at the $LaAlO_3$/$SrTiO_3$ heterointerface. *Nature* 427:423–26

2. Basletic M, Maurice JL, Carretero C, Herranz G, Copie O, et al. 2008. Mapping the spatial distribution of charge carriers in $LaAlO_3/SrTiO_3$ heterostructures. *Nat. Mater.* 7:621–25

3. Kalisky B, Spanton EM, Noad H, Kirtley JR, Nowack KC, et al. 2013. Locally enhanced conductivity due to the tetragonal domain structure in $LaAlO_3/SrTiO_3$ heterointerfaces. *Nat. Mater.* 12:1091–95

4. Honig M, Sulpizio JA, Drori J, Joshua A, Zeldov E, Ilani S. 2013. Local electrostatic imaging of striped domain order in $LaAlO_3/SrTiO_3$. *Nat. Mater.* 12:1112–18

5. Cheng GL, Siles PF, Bi F, Cen C, Bogorin DF, et al. 2011. Sketched oxide single-electron transistor. *Nat. Nanotechnol.* 6:343–47

6. Cheng G, Veazey JP, Irvin P, Cen C, Bogorin DF, et al. 2013. Anomalous transport in sketched nanostructures at the $LaAlO_3/SrTiO_3$ interface. *Phys. Rev. X* 3:011021

7. Müller KA, Berlinger W, Waldner F. 1968. Characteristic structural phase transition in perovskite-type compounds. *Phys. Rev. Lett.* 21:814–17

8. Fleury PA, Scott JF, Worlock JM. 1968. Soft phonon modes and the 110°K phase transition in $SrTiO_3$. *Phys. Rev. Lett.* 21:16–19

9. Lytle FW. 1964. X ray diffractometry of low temperature phase transformations in strontium titanate. *J. Appl. Phys.* 35:2212–15

10. Sawaguchi E, Kikuchi A, Kodera Y. 1963. Microscopic examination of $SrTiO_3$ at low temperatures. *J. Phys. Soc. Jpn.* 18:459

11. Zhong V, Tóth A, Held K. 2013. Theory of spin-orbit coupling at $LaAlO_3/SrTiO_3$ interfaces and $SrTiO_3$ surfaces. *Phys. Rev. B* 87:161102(R)

12. Bistritzer R, Khalsa G, MacDonald AH. 2011. Electronic structure of doped d^0 perovskite semiconductors. *Phys. Rev. B* 83:115114

13. Itoh M, Wang R, Inaguma Y, Yamaguchi T, Shan YJ, Nakamura T. 1999. Ferroelectricity induced by oxygen isotope exchange in strontium titanate perovskite. *Phys. Rev. Lett.* 82:3540–43

14. Müller KA, Burkard H. 1979. $SrTiO_3$: an intrinsic quantum paraelectric below 4 K. *Phys. Rev. B* 19:3593–602

15. Sakudo T, Unoki H. 1971. Dielectric properties of $SrTiO_3$ at low temperatures. *Phys. Rev. Lett.* 26:851–53

16. Haeni JH, Irvin P, Chang W, Uecker R, Reiche P, et al. 2004. Room-temperature ferroelectricity in strained $SrTiO_3$. *Nature* 430:758–61

17. Kim YS, Kim DJ, Kim TH, Noh TW, Choi JS, et al. 2007. Observation of room-temperature ferroelectricity in tetragonal strontium titanate thin films on $SrTiO_3$ (001) substrates. *Appl. Phys. Lett.* 91:042908

18. Koonce CS, Cohen ML, Schooley JF, Hosler WR, Pfeiffer ER. 1967. Superconducting transition temperatures of semiconducting $SrTiO_3$. *Phys. Rev.* 163:380–90

19. Brinkman A, Huijben M, Van Zalk M, Huijben J, Zeitler U, et al. 2007. Magnetic effects at the interface between non-magnetic oxides. *Nat. Mater.* 6:493–96

20. Moetakef P, Williams JR, Ouellette DG, Kajdos AP, Goldhaber-Gordon D, et al. 2012. Carrier-controlled ferromagnetism in $SrTiO_3$. *Phys. Rev. X* 2:021014

21. Bert JA, Kalisky B, Bell C, Kim M, Hikita Y, et al. 2011. Direct imaging of the coexistence of ferromagnetism and superconductivity at the $LaAlO_3/SrTiO_3$ interface. *Nat. Phys.* 7:767–71

22. Ariando, Wang X, Baskaran G, Liu ZQ, Huijben J, et al. 2011. Electronic phase separation at the $LaAlO_3/SrTiO_3$ interface. *Nat. Commun.* 2:1192

23. Dikin DA, Mehta M, Bark CW, Folkman CM, Eom CB, Chandrasekhar V. 2011. Coexistence of superconductivity and ferromagnetism in two dimensions. *Phys. Rev. Lett.* 107:056802

24. Li L, Richter C, Mannhart J, Ashoori RC. 2011. Coexistence of magnetic order and two-dimensional superconductivity at $LaAlO_3/SrTiO_3$ interfaces. *Nat. Phys.* 7:762–66

25. Kalisky B, Bert JA, Klopfer BB, Bell C, Sato HK, et al. 2012. Critical thickness for ferromagnetism in $LaAlO_3/SrTiO_3$ heterostructures. *Nat. Commun.* 3:922

26. Fitzsimmons MR, Hengartner NW, Singh S, Zhernenkov M, Bruno FY, et al. 2011. Upper limit to magnetism in $LaAlO_3/SrTiO_3$ heterostructures. *Phys. Rev. Lett.* 107:217201

27. Salman Z, Ofer O, Radovic M, Hao H, Ben Shalom M, et al. 2012. Nature of weak magnetism in $SrTiO_3/LaAlO_3$ multilayers. *Phys. Rev. Lett.* 109:257207

28. Lee JS, Xie YW, Sato HK, Bell C, Hikita Y, et al. 2013. Titanium d_{xy} ferromagnetism at the LaAlO$_3$/SrTiO$_3$ interface. *Nat. Mater.* 12:703–6

29. Pentcheva R, Pickett WE. 2006. Charge localization or itineracy at LaAlO$_3$/SrTiO$_3$ interfaces: hole polarons, oxygen vacancies, and mobile electrons. *Phys. Rev. B* 74:035112

30. Kalisky B, Bert JA, Bell C, Xie YW, Sato HK, et al. 2012. Scanning probe manipulation of magnetism at the LaAlO$_3$/SrTiO$_3$ heterointerface. *Nano Lett.* 12:4055–59

31. Pavlenko N, Kopp T, Tsymbal EY, Sawatzky GA, Mannhart J. 2012. Magnetic and superconducting phases at the LaAlO$_3$/SrTiO$_3$ interface: the role of interfacial Ti 3d electrons. *Phys. Rev. B* 85:020407(R)

32. Joshua A, Ruhman J, Pecker S, Altman E, Ilani S. 2013. Gate-tunable polarized phase of two-dimensional electrons at the LaAlO$_3$/SrTiO$_3$ interface. *Proc. Natl. Acad. Sci. USA* 110:9633–38

33. Flekser E, Ben Shalom M, Kim M, Bell C, Hikita Y, et al. 2012. Magnetotransport effects in polar versus non-polar SrTiO$_3$ based heterostructures. *Phys. Rev. B* 86:121104

34. Seri S, Klein L. 2009. Antisymmetric magnetoresistance of the SrTiO$_3$/LaAlO$_3$ interface. *Phys. Rev. B* 80:180410

35. Bi F, Huang M, Bark C-W, Ryu S, Eom C-B, et al. 2013. Room-temperature electronically-controlled ferromagnetism at the LaAlO$_3$/SrTiO$_3$ interface. arXiv:1307.5557

36. Moetakef P, Williams JR, Ouellette DG, Kajdos AP, Goldhaber-Gordon D, et al. 2013. Carrier-controlled ferromagnetism in SrTiO$_3$. *Phys. Rev. X* 2:021014

37. Mattheiss LF. 1972. Energy bands for KNiF$_3$, SrTiO$_3$, KMoO$_3$, and KTaO$_3$. *Phys. Rev. B* 6:4718–40

38. Hilgenkamp H. 2013. Novel transport phenomena at complex oxide interfaces. *MRS Bull.* 38:1026–31

39. Nakagawa N, Hwang HY, Muller DA. 2006. Why some interfaces cannot be sharp. *Nat. Mater.* 5:204–9

40. Thiel S, Hammerl G, Schmehl A, Schneider CW, Mannhart J. 2006. Tunable quasi-two-dimensional electron gases in oxide heterostructures. *Science* 313:1942–45

41. Warusawithana MP, Richter C, Mundy JA, Roy P, Ludwig J, et al. 2013. LaAlO$_3$ stoichiometry is key to electron liquid formation at LaAlO$_3$/SrTiO$_3$ interfaces. *Nat. Commun.* 4:2351

42. Dildar IM, Boltje DB, Hesselberth MHS, Aarts J, Xu Q, et al. 2013. Non-conducting interfaces of LaAlO$_3$/SrTiO$_3$ produced in sputter deposition: the role of stoichiometry. *Appl. Phys. Lett.* 102:121601

43. Breckenfeld E, Bronn N, Karthik J, Damodaran AR, Lee S, et al. 2013. Effect of growth induced (non)stoichiometry on interfacial conductance in LaAlO$_3$/SrTiO$_3$. *Phys. Rev. Lett.* 110:196804

44. Sato HK, Bell C, Hikita Y, Hwang HY. 2013. Stoichiometry control of the electronic properties of the LaAlO$_3$/SrTiO$_3$ heterointerface. *Appl. Phys. Lett.* 102:251602

45. Lee SW, Liu Y, Heo J, Gordon RG. 2012. Creation and control of two-dimensional electron gas using Al-based amorphous oxides/SrTiO$_3$ heterostructures grown by atomic layer deposition. *Nano Lett.* 12:4775–83

46. Chen Y, Pryds N, Kleibeuker JE, Koster G, Sun J, et al. 2011. Metallic and insulating interfaces of amorphous SrTiO$_3$-based oxide heterostructures. *Nano Lett.* 11:3774–78

47. Chen YZ, Bovet N, Trier F, Christensen DV, Qu FM, et al. 2013. A high-mobility two-dimensional electron gas at the spinel/perovskite interface of γ-Al$_2$O$_3$/SrTiO$_3$. *Nat. Commun.* 4:1371

48. Ueno K, Nakamura S, Shimotani H, Ohtomo A, Kimura N, et al. 2008. Electric-field-induced super-conductivity in an insulator. *Nat. Mater.* 7:855–58

49. Lee Y, Clement C, Hellerstedt J, Kinney J, Kinnischtzke L, et al. 2011. Phase diagram of electrostatically doped SrTiO$_3$. *Phys. Rev. Lett.* 106:136809

50. Sekiya D, Nakamura H, Kimura T. 2011. Enhanced carrier injection in perovskite field-effect transistors via low-barrier contacts. *App. Phys. Express* 4:064103

51. Nakamura H, Koga T, Kimura T. 2012. Experimental evidence of cubic Rashba effect in an inversion-symmetric oxide. *Phys. Rev. Lett.* 108:206601

52. Santander-Syro AF, Copie O, Kondo T, Fortuna F, Pailhes S, et al. 2011. Two-dimensional electron gas with universal subbands at the surface of SrTiO$_3$. *Nature* 469:189–93

53. Meevasana W, King PDC, He RH, Mo SK, Hashimoto M, et al. 2011. Creation and control of a two-dimensional electron liquid at the bare SrTiO$_3$ surface. *Nat. Mater.* 10:114–18

54. Huang B-C, Chiu Y-P, Huang P-C, Wang W-C, Tra VT, et al. 2012. Mapping band alignment across complex oxide heterointerfaces. *Phys. Rev. Lett.* 109:246807

55. Kalabukhov A, Gunnarsson R, Börjesson J, Olsson E, Claeson T, Winkler D. 2007. Effect of oxygen vacancies in the $SrTiO_3$ substrate on the electrical properties of the $LaAlO_3/SrTiO_3$ interface. *Phys. Rev. B* 75:121404

56. Yu L, Zunger A. 2014. A unified mechanism for conductivity and magnetism at interfaces of insulating nonmagnetic oxides. arXiv:1402.0895

57. Siemons W, Koster G, Yamamoto H, Harrison WA, Lucovsky G, et al. 2007. Origin of charge density at $LaAlO_3$ on $SrTiO_3$ heterointerfaces: possibility of intrinsic doping. *Phys. Rev. Lett.* 98:196802

58. Qiao L, Droubay TC, Kaspar TC, Sushko PV, Chambers SA. 2011. Cation mixing, band offsets and electric fields at $LaAlO_3/SrTiO_3$ (001) heterojunctions with variable La:Al atom ratio. *Surf. Sci.* 605:1381–87

59. Willmott PR, Pauli SA, Herger R, Schlepütz CM, Martoccia D, et al. 2007. Structural basis for the conducting interface between $LaAlO_3$ and $SrTiO_3$. *Phys. Rev. Lett.* 99:155502

60. Baraff GA, Appelbaum JA, Hamann DR. 1977. Self-consistent calculation of the electronic structure at an abrupt GaAs-Ge interface. *Phys. Rev. Lett.* 38:237–40

61. Harrison WA, Kraut EA, Waldrop JR, Grant RW. 1978. Polar heterojunction interfaces. *Phys. Rev. B* 18:4402–10

62. Kroemer H. 1987. Polar-on-nonpolar epitaxy. *J. Cryst. Growth* 81:193–204

63. Singh-Bhalla G, Bell C, Ravichandran J, Siemons W, Hikita Y, et al. 2011. Built-in and induced polarization across $LaAlO_3/SrTiO_3$ heterojunctions. *Nat. Phys.* 7:80–86

64. Reinle-Schmitt ML, Cancellieri C, Li D, Fontaine D, Medarde M, et al. 2012. Tunable conductivity threshold at polar oxide interfaces. *Nat. Commun.* 3:932

65. Cancellieri C, Fontaine D, Gariglio S, Reyren N, Caviglia AD, et al. 2011. Electrostriction at the $LaAlO_3/SrTiO_3$ interface. *Phys. Rev. Lett.* 107:056102

66. Liu ZQ, Li CJ, Lü WM, Huang XH, Huang Z, et al. 2013. Origin of the two-dimensional electron gas at $LaAlO_3/SrTiO_3$ interfaces: the role of oxygen vacancies and electronic reconstruction. *Phys. Rev. X* 3:021010

67. Förg B, Richter C, Mannhart J. 2012. Field-effect devices utilizing $LaAlO_3$-$SrTiO_3$ interfaces. *Appl. Phys. Lett.* 100:053506

68. Tra VT, Chen J-W, Huang P-C, Huang B-C, Cao Y, et al. 2013. Ferroelectric control of the conduction at the $LaAlO_3/SrTiO_3$ heterointerface. *Adv. Mater.* 25:3357–64

69. Xie Y, Hikita Y, Bell C, Hwang HY. 2011. Control of electronic conduction at an oxide heterointerface using surface polar adsorbates. *Nat. Commun.* 2:494

70. Schneider CW, Thiel S, Hammerl G, Richter C, Mannhart J. 2006. Microlithography of electron gases formed at interfaces in oxide heterostructures. *Appl. Phys. Lett.* 89:122101

71. Stornaiuolo D, Gariglio S, Couto NJG, Fête A, Caviglia AD, et al. 2012. In-plane electronic confinement in superconducting $LaAlO_3/SrTiO_3$ nanostructures. *Appl. Phys. Lett.* 101:222601

72. Aurino PP, Kalabukhov A, Tuzla N, Olsson E, Claeson T, Winkler D. 2013. Nano-patterning of the electron gas at the $LaAlO_3/SrTiO_3$ interface using low-energy ion beam irradiation. *Appl. Phys. Lett.* 102:201610

73. Mathew S, Annadi A, Chan TK, Asmara TC, Zhan D, et al. 2013. Tuning the interface conductivity of $LaAlO_3/SrTiO_3$ using ion beams: implications for patterning. *ACS Nano* 7:10572–81

74. Cen C, Thiel S, Hammerl G, Schneider CW, Andersen KE, et al. 2008. Nanoscale control of an interfacial metal-insulator transition at room temperature. *Nat. Mater.* 7:298–302

75. Xie Y, Bell C, Hikita Y, Hwang HY. 2011. Tuning the electron gas at an oxide heterointerface via free surface charges. *Adv. Mater.* 23:1744

76. Bi F, Bogorin DF, Cen C, Bark CW, Park JW, et al. 2010. "Water-cycle" mechanism for writing and erasing nanostructures at the $LaAlO_3/SrTiO_3$ interface. *Appl. Phys. Lett.* 97:173110

77. Huang M, Bi F, Ryu S, Eom C-B, Irvin P, Levy J. 2013. Direct imaging of $LaAlO_3/SrTiO_3$ nanostructures using piezoresponse force microscopy. *APL Mater.* 1:052110

78. Xie Y, Bell C, Yajima T, Hikita Y, Hwang HY. 2010. Charge writing at the $LaAlO_3/SrTiO_3$ surface. *Nano Lett.* 10:2588–91

79. Hwang HY, Iwasa Y, Kawasaki M, Keimer B, Nagaosa N, Tokura Y. 2012. Emergent phenomena at oxide interfaces. *Nat. Mater.* 11:103–13

80. Liao YC, Kopp T, Richter C, Rosch A, Mannhart J. 2011. Metal-insulator transition of the $LaAlO_3$-$SrTiO_3$ interface electron system. *Phys. Rev. B* 83:075402

81. Bell C, Harashima S, Kozuka Y, Kim M, Kim BG, et al. 2009. Dominant mobility modulation by the electric field effect at the $LaAlO_3/SrTiO_3$ interface. *Phys. Rev. Lett.* 103:226802

82. Caviglia AD, Gariglio S, Cancellieri C, Sacepe B, Fête A, et al. 2010. Two-dimensional quantum oscillations of the conductance at $LaAlO_3/SrTiO_3$ interfaces. *Phys. Rev. Lett.* 105:236802

83. Ben Shalom M, Ron A, Palevski A, Dagan Y. 2010. Shubnikov–de Haas oscillations in $SrTiO_3/LaAlO_3$ interface. *Phys. Rev. Lett.* 105:206401

84. Pentcheva R, Huijben M, Otte K, Pickett WE, Kleibeuker JE, et al. 2010. Parallel electron-hole bilayer conductivity from electronic interface reconstruction. *Phys. Rev. Lett.* 104:166804

85. Kim JS, Seo SSA, Chisholm MF, Kremer RK, Habermeier HU, et al. 2010. Nonlinear Hall effect and multichannel conduction in $LaTiO_3/SrTiO_3$ superlattices. *Phys. Rev. B* 82:201407

86. Lerer S, Ben Shalom M, Deutscher G, Dagan Y. 2011. Low-temperature dependence of the thermomagnetic transport properties of the $SrTiO_3/LaAlO_3$ interface. *Phys. Rev. B* 84:075423

87. Biscaras J, Bergeal N, Hurand S, Grossetete C, Rastogi A, et al. 2012. Two-dimensional superconducting phase in $LaTiO_3/SrTiO_3$ heterostructures induced by high-mobility carrier doping. *Phys. Rev. Lett.* 108:247004

88. Brinks P, Siemons W, Kleibeuker JE, Koster G, Rijnders G, Huijben M. 2011. Anisotropic electrical transport properties of a two-dimensional electron gas at $SrTiO_3$-$LaAlO_3$ interfaces. *Appl. Phys. Lett.* 98:242904

89. Ben Shalom M, Tai CW, Lereah Y, Sachs M, Levy E, et al. 2009. Anisotropic magnetotransport at the $SrTiO_3/LaAlO_3$ interface. *Phys. Rev. B* 80:140403

90. Annadi A, Huang Z, Gopinadhan K, Wang XR, Srivastava A, et al. 2013. Fourfold oscillation in anisotropic magnetoresistance and planar Hall effect at the $LaAlO_3/SrTiO_3$ heterointerfaces: effect of carrier confinement and electric field on magnetic interactions. *Phys. Rev. B* 87:201102

91. Caviglia AD, Gabay M, Gariglio S, Reyren N, Cancellieri C, Triscone JM. 2010. Tunable Rashba spin-orbit interaction at oxide interfaces. *Phys. Rev. Lett.* 104:126803

92. Fête A, Gariglio S, Caviglia AD, Triscone JM, Gabay M. 2012. Rashba induced magnetoconductance oscillations in the $LaAlO_3$-$SrTiO_3$ heterostructure. *Phys. Rev. B* 86:201105

93. Ben Shalom M, Sachs M, Rakhmilevitch D, Palevski A, Dagan Y. 2010. Tuning spin-orbit coupling and superconductivity at the $SrTiO_3/LaAlO_3$ interface: a magnetotransport study. *Phys. Rev. Lett.* 104:126802

94. Joshua A, Pecker S, Ruhman J, Altman E, Ilani S. 2012. A universal critical density underlying the physics of electrons at the $LaAlO_3/SrTiO_3$ interface. *Nat. Commun.* 3:1129

95. Khalsa G, Lee B, MacDonald AH. 2013. Theory of t_{2g} electron-gas Rashba interactions. *Phys. Rev. B* 88:041302(R)

96. Mannhart J, Blank DHA, Hwang HY, Millis AJ, Triscone JM. 2008. Two-dimensional electron gases at oxide interfaces. *MRS Bull.* 33:1027–34

97. Cancellieri C, Reinle-Schmitt ML, Kobayashi M, Strocov VN, Fontaine D, et al. 2014. Doping-dependent band structure of $LaAlO_3/SrTiO_3$ interfaces by soft X-ray polarization-controlled resonant angle-resolved photoemission. *Phys. Rev. B* 89:121412(R)

98. Kim Y, Lutchyn RM, Nayak C. 2013. Origin and transport signatures of spin-orbit interactions in one- and two-dimensional $SrTiO_3$-based heterostructures. *Phys. Rev. B* 87:245121

99. Fischer MH, Raghu S, Kim EA. 2013. Spin-orbit coupling in $LaAlO_3/SrTiO_3$ interfaces: magnetism and orbital ordering. *New J. Phys.* 15:023022

100. Lin X, Zhu Z, Fauqué B, Behnia K. 2013. Fermi surface of the most dilute superconductor. *Phys. Rev. X* 3:021002

101. Bednorz JG, Müller KA. 1987. Perovskite-type oxides—the new approach to high-T_c superconductivity. *Rev. Mod. Phys.* 60:585–600

102. Schooley JF, Hosler WR, Ambler E, Becker JH, Cohen ML, Koonce CS. 1965. Dependence of the superconducting transition temperature on carrier concentration in semiconducting $SrTiO_3$. *Phys. Rev. Lett.* 14:305–7

103. Cohen ML. 1964. The existence of a superconducting state in semiconductors. *Rev. Mod. Phys.* 36:240–43

104. Schooley JF, Hosler WR, Cohen ML. 1964. Superconductivity in semiconducting $SrTiO_3$. *Phys. Rev. Lett.* 12:474–75

105. Binnig G, Baratoff A, Hoenig HE, Bednorz JG. 1980. Two-band superconductivity in Nb-doped $SrTiO_3$. *Phys. Rev. Lett.* 45:1352–55

106. Fernandes RM, Haraldsen JT, Wölfle P, Balatsky AV. 2013. Two-band superconductivity in doped $SrTiO_3$ films and interfaces. *Phys. Rev. B* 87:014510

107. Fulde P, Farrell RA. 1964. Superconductivity in a strong spin-exchange field. *Phys. Rev.* 135:A550–63

108. Larkin AI, Ovchinikov YN. 1965. Nonuniform state of superconductors. *Sov. Phys. JETP* 20:762

109. Michaeli K, Potter AC, Lee PA. 2012. Superconducting and ferromagnetic phases in $SrTiO_3$/$LaAlO_3$ oxide interface structures: possibility of finite momentum pairing. *Phys. Rev. Lett.* 108:117003

110. Reyren N, Thiel S, Caviglia AD, Kourkoutis LF, Hammerl G, et al. 2007. Superconducting interfaces between insulating oxides. *Science* 317:1196–99

111. Caviglia AD, Gariglio S, Reyren N, Jaccard D, Schneider T, et al. 2008. Electric field control of the $LaAlO_3$/$SrTiO_3$ interface ground state. *Nature* 456:624–27

112. Richter C, Boschker H, Dietsche W, Fillis-Tsirakis E, Jany R, et al. 2013. Interface superconductor with gap behaviour like a high-temperature superconductor. *Nature* 502:528–31

113. Bert JA, Nowack KC, Kalisky B, Noad H, Kirtley JR, et al. 2012. Gate-tuned superfluid density at the superconducting $LaAlO_3$/$SrTiO_3$ interface. *Phys. Rev. B* 86:060503

114. Reyren N, Gariglio S, Caviglia AD, Jaccard D, Schneider T, Triscone JM. 2009. Anisotropy of the superconducting transport properties of the $LaAlO_3$/$SrTiO_3$ interface. *Appl. Phys. Lett.* 94:112506

115. Gardner HJ, Kumar A, Yu L, Xiong P, Warusawithana MP, et al. 2011. Enhancement of superconductivity by a parallel magnetic field in two-dimensional superconductors. *Nat. Phys.* 7:895–900

116. Fidkowski L, Jiang H-C, Lutchyn RM, Nayak C. 2013. Magnetic and superconducting ordering in one-dimensional nanostructures at the $LaAlO_3$/$SrTiO_3$ interface. *Phys. Rev. B* 87:014436

117. Veazey JP, Cheng G, Irvin P, Cen C, Bogorin DF, et al. 2013. Oxide-based platform for reconfigurable superconducting nanoelectronics. *Nanotechnology* 24:375201

118. Tang HX, Kawakami RK, Awschalom DD, Roukes ML. 2003. Giant planar Hall effect in epitaxial (Ga,Mn)As devices. *Phys. Rev. Lett.* 90:107201

119. Bason Y, Klein L, Yau J-B, Hong X, Ahn CH. 2004. Giant planar Hall effect in colossal magnetoresistive $La_{0.84}Sr_{0.16}MnO_3$ thin films. *Appl. Phys. Lett.* 84:2593–95

120. Chen G, Balents L. 2013. Ferromagnetism in itinerant two-dimensional t_{2g} systems. *Phys. Rev. Lett.* 110:206401

121. Banerjee S, Erten O, Randeria M. 2013. Ferromagnetic exchange, spin-orbit coupling and spiral magnetism at the $LaAlO_3$/$SrTiO_3$ interface. *Nat. Phys.* 9:626–30

122. Ruhman J, Joshua A, Ilani S, Altman E. 2013. Competition between Kondo screening and magnetism at the $LaAlO_3$/$SrTiO_3$ interface. arXiv:1311.4541v1

123. Li X, Liu WV, Balents L. 2014. Spirals and skyrmions in two dimensional oxide heterostructures. *Phys. Rev. Lett.* 112:067202

124. Anderson PW, Hasegawa H. 1955. Considerations on double exchange. *Phys. Rev.* 100:675–81

125. de Gennes PG. 1960. Effects of double exchange in magnetic crystals. *Phys. Rev.* 118:141–54

126. Cowley RA. 1964. Lattice dynamics and phase transitions of strontium titanate. *Phys. Rev.* 134:A981–97

127. Dec J, Kleemann W, Itoh M. 2004. Electric-field-induced ferroelastic single domaining of $SrTi^{18}O_3$. *Appl. Phys. Lett.* 85:5328–30

128. Scott JF, Salje EKH, Carpenter MA. 2012. Domain wall damping and elastic softening in $SrTiO_3$: evidence for polar twin walls. *Phys. Rev. Lett.* 109:187601

129. Zubko P, Catalan G, Buckley A, Welche PRL, Scott JF. 2007. Strain-gradient-induced polarization in $SrTiO_3$ single crystals. *Phys. Rev. Lett.* 99:167601

130. Morozovska AN, Eliseev EA, Glinchuk MD, Chen L-Q, Gopalan V. 2012. Interfacial polarization and pyroelectricity in antiferrodistortive structures induced by a flexoelectric effect and rotostriction. *Phys. Rev. B* 85:094107

131. Grupp DE, Goldman AM. 1997. Giant piezoelectric effect in strontium titanate at cryogenic temperatures. *Science* 276:392–94

132. Bell C, Harashima S, Hikita Y, Hwang HY. 2009. Thickness dependence of the mobility at the LaAlO$_3$/SrTiO$_3$ interface. *Appl. Phys. Lett.* 94:222111

133. Seidel J, Martin LW, He Q, Zhan Q, Chu YH, et al. 2009. Conduction at domain walls in oxide multiferroics. *Nat. Mater.* 8:229–34

134. Catalan G, Seidel J, Ramesh R, Scott JF. 2012. Domain wall nanoelectronics. *Rev. Mod. Phys.* 84:119–56

135. Yang Z, Ko C, Ramanathan S. 2011. Oxide electronics utilizing ultrafast metal-insulator transitions. *Annu. Rev. Mater. Res.* 41:337–67

136. Kälblein D, Weitz RT, Böttcher HJ, Ante F, Zschieschang U, et al. 2011. Top-gate ZnO nanowire transistors and integrated circuits with ultrathin self-assembled monolayer gate dielectric. *Nano Lett.* 11:5309–15

137. Li L, Richter C, Paetel S, Kopp T, Mannhart J, Ashoori RC. 2011. Very large capacitance enhancement in a two-dimensional electron system. *Science* 332:825–28

138. Jany R, Breitschaft M, Hammerl G, Horsche A, Richter C, et al. 2010. Diodes with breakdown voltages enhanced by the metal-insulator transition of LaAlO$_3$-SrTiO$_3$ interfaces. *Appl. Phys. Lett.* 96:183504

139. Jany R, Richter C, Woltmann C, Pfanzelt G, Förg B, et al. 2014. Monolithically integrated circuits from functional oxides. *Adv. Mater. Interfaces* 1:1300031

140. Stone AD. 1985. Magnetoresistance fluctuations in mesoscopic wires and rings. *Phys. Rev. Lett.* 54:2692–95

141. Webb RA, Washburn S, Umbach CP, Laibowitz RB. 1985. Observation of h/e Aharonov-Bohm oscillations in normal-metal rings. *Phys. Rev. Lett.* 54:2696–99

142. Rakhmilevitch D, Ben Shalom M, Eshkol M, Tsukernik A, Palevski A, Dagan Y. 2010. Phase coherent transport in SrTiO$_3$/LaAlO$_3$ interfaces. *Phys. Rev. B* 82:235119

143. Rakhmilevitch D, Neder I, Shalom MB, Tsukernik A, Karpovski M, et al. 2013. Anomalous response to gate voltage application in mesoscopic LaAlO$_3$/SrTiO$_3$ devices. *Phys. Rev. B* 87:125409

144. Irvin P, Veazey JP, Cheng G, Lu S, Bark C-W, et al. 2013. Anomalous high mobility in LaAlO$_3$/SrTiO$_3$ nanowires. *Nano Lett.* 13:364–68

145. Bogorin DF, Bark CW, Jang HW, Cen C, Folkman CM, et al. 2010. Nanoscale rectification at the LaAlO$_3$/SrTiO$_3$ interface. *Appl. Phys. Lett.* 97:013102

146. Srinivasa V, Levy J. 2012. Spatial analogue of quantum spin dynamics via spin-orbit interaction. arXiv:1111.5311

147. Cen C, Bogorin DF, Levy J. 2010. Thermal activation and quantum field emission in a sketch-based oxide nanotransistor. *Nanotechnology* 21:475201

148. Veazey JP, Cheng G, Lu S, Tomczyk M, Bi F, et al. 2013. Nonlocal current-voltage characteristics of gated superconducting sketched oxide nanostructures. *Europhys. Lett.* 103:57001

149. Clarke J. 1972. Experimental observation of pair-quasiparticle potential difference in nonequilibrium superconductors. *Phys. Rev. Lett.* 28:1363–66

150. Cadden-Zimansky P, Chandrasekhar V. 2006. Nonlocal correlations in normal-metal superconducting systems. *Phys. Rev. Lett.* 97:237003

151. Oreg Y, Refael G, von Oppen F. 2010. Helical liquids and Majorana bound states in quantum wires. *Phys. Rev. Lett.* 105:177002

152. Lutchyn RM, Sau JD, Das Sarma S. 2010. Majorana fermions and a topological phase transition in semiconductor-superconductor heterostructures. *Phys. Rev. Lett.* 105:077001

153. Cen C, Thiel S, Mannhart J, Levy J. 2009. Oxide nanoelectronics on demand. *Science* 323:1026–30

154. Irvin P, Huang M, Wong FJ, Sanders TD, Suzuki Y, Levy J. 2013. Gigahertz-frequency operation of a LaAlO$_3$/SrTiO$_3$-based nanotransistor. *Appl. Phys. Lett.* 102:103113

155. Irvin P, Ma YJ, Bogorin DF, Cen C, Bark CW, et al. 2010. Rewritable nanoscale oxide photodetector. *Nat. Photonics* 4:849–52

156. Ma Y, Huang M, Ryu S, Bark CW, Eom C-B, et al. 2013. Broadband terahertz generation and detection at 10 nm scale. *Nano Lett.* 13:2884–88

157. Kastner MA. 1992. The single-electron transistor. *Rev. Mod. Phys.* 64:849–58

158. Son J, Moetakef P, Jalan B, Bierwagen O, Wright NJ, et al. 2010. Epitaxial SrTiO$_3$ films with electron mobilities exceeding 30,000 cm^2 V^{-1} s^{-1}. *Nat. Mater.* 9:482–84

159. Vasyukov D, Anahory Y, Embon L, Halbertal D, Cuppens J, et al. 2013. A scanning superconducting quantum interference device with single electron spin sensitivity. *Nat. Nanotechnol.* 8:639–44

160. Liu MK, Wagner M, Abreu E, Kittiwatanakul S, McLeod A, et al. 2013. Anisotropic electronic state via spontaneous phase separation in strained vanadium dioxide films. *Phys. Rev. Lett.* 111:096602

161. Lai K, Kundhikanjana W, Kelly MA, Shen Z-X, Shabani J, Shayegan M. 2011. Imaging of coulomb-driven quantum Hall edge states. *Phys. Rev. Lett.* 107:176809

162. Pfeiffer L, West KW. 2003. The role of MBE in recent quantum Hall effect physics discoveries. *Phys. E* 20:57–64

163. Umansky V, Heiblum M, Levinson Y, Smet J, Nübler J, Dolev M. 2009. MBE growth of ultra-low disorder 2DEG with mobility exceeding 35×10^6 cm^2/V s. *J. Cryst. Growth* 311:1658–61

164. Morozov SV, Novoselov KS, Katsnelson MI, Schedin F, Elias DC, et al. 2008. Giant intrinsic carrier mobilities in graphene and its bilayer. *Phys. Rev. Lett.* 100:016602

165. Bolotin KI, Sikes KJ, Jiang Z, Klima M, Fudenberg G, et al. 2008. Ultrahigh electron mobility in suspended graphene. *Solid State Commun.* 146:351–55

166. Du X, Skachko I, Barker A, Andrei EY. 2008. Approaching ballistic transport in suspended graphene. *Nat. Nanotechnol.* 3:491–95

167. Dürkop T, Getty SA, Cobas E, Fuhrer MS. 2003. Extraordinary mobility in semiconducting carbon nanotubes. *Nano Lett.* 4:35–39

168. Ford AC, Ho JC, Chueh Y-L, Tseng Y-C, Fan Z, et al. 2008. Diameter-dependent electron mobility of InAs nanowires. *Nano Lett.* 9:360–65

169. Purewal MS, Hong BH, Ravi A, Chandra B, Hone J, Kim P. 2007. Scaling of resistance and electron mean free path of single-walled carbon nanotubes. *Phys. Rev. Lett.* 98:186808

170. Chuang S, Gao Q, Kapadia R, Ford AC, Guo J, Javey A. 2012. Ballistic InAs nanowire transistors. *Nano Lett.* 13:555–58

171. Held R, Heinzel T, Studerus P, Ensslin K, Holland M. 1997. Semiconductor quantum point contact fabricated by lithography with an atomic force microscope. *Appl. Phys. Lett.* 71:2689–91

172. Waissman J, Honig M, Pecker S, Benyamini A, Hamo A, Ilani S. 2013. Realization of pristine and locally tunable one-dimensional electron systems in carbon nanotubes. *Nat. Nanotechnol.* 8:569–74

173. Dietl T. 2010. A ten-year perspective on dilute magnetic semiconductors and oxides. *Nat. Mater.* 9:965–74

174. Kuemmeth F, Ilani S, Ralph DC, McEuen PL. 2008. Coupling of spin and orbital motion of electrons in carbon nanotubes. *Nature* 452:448–52

175. Jespersen TS, Grove-Rasmussen K, Paaske J, Muraki K, Fujisawa T, et al. 2011. Gate-dependent spin-orbit coupling in multielectron carbon nanotubes. *Nat. Phys.* 7:348–53

176. Steele GA, Pei F, Laird EA, Jol JM, Meerwaldt HB, Kouwenhoven LP. 2013. Large spin-orbit coupling in carbon nanotubes. *Nat. Commun.* 4:1573

Contents

Index

Errata

An online log of corrections to *Annual Review of Materials Research* articles may be found at http://www.annualreviews.org/errata/matsci